Upper Crustal Control on Nearshore Subduction Mechanics in Cascadia

Asif Ashraf,[1] Emilie E.E. Hooft,[1] Douglas R. Toomey[1]

[1] Department of Earth Sciences, University of Oregon, Eugene, OR-97403, USA

Corresponding Author: Asif Ashraf (aashraf@uoregon.edu)

Abstract

Along-strike upper plate heterogeneity is widely observed at subduction margins, but its direct influence on slab geometry and interseismic deformation remains debated. Here, we investigate the effect of upper-crustal geological segmentation on nearshore subduction mechanics at the Cascadia margin. Using a high-resolution, shore-crossing 3-D seismic tomography model from central to southern Oregon, we image sharp along-strike contrasts in upper-crustal velocity associated with distinct accreted terranes. We show that the subducting slab is systematically deeper beneath the coherent, high-velocity Siletz terrane and shallower beneath low-velocity faulted Siletz and Franciscan terranes. Numerical simulations constrained by the tomographic velocities demonstrate that upper-plate density and rigidity contrasts alone reproduce the observed variation in slab depth and, when combined with viscoelastic deformation, explain the magnitude and pattern of coastal uplift. These findings establish that the along-strike changes in upper-crustal backstop, despite being ignored in geodetic locking models, are a primary mechanical filter that organizes subduction zone architecture and regulates the accumulation of megathrust related strain.

Teaser

Upper crustal geology shapes how the Cascadia slab bends and uplifts the coast, revealing structure-driven segmentation of subduction mechanics.

INTRODUCTION

The last megathrust earthquake at the Cascadia Subduction Zone (CSZ) occurred in 1700 (*1*). Given an estimated average recurrence interval of approximately 300-500 years (*2*), the system is likely approaching the end of the current interseismic period. During this phase, both the upper and lower crust undergo significant deformation (*3*). Characterizing this ongoing accumulation of strain is critical for understanding future megathrust ruptures, as it provides essential constraints on the mechanics of the subduction system. This study investigates two distinct modes of nearshore crustal deformation at CSZ: flexural bending of the subducting slab and upper-plate uplift rates at the coast. We focus on the along-strike segmentation of these interseismic deformation modes to evaluate if upper crustal geological heterogeneity drives the observed along-strike variability in slab bending and coastal uplift rates (both interseismic and long-term), as suggested by several previous observations (*4–6*).

Contemporary interpretations of subduction mechanics frequently overlook the influence of upper-crustal geologic variability. For example, geodetic locking models of the CSZ (*7–9*), whether utilizing analytical elastic half-space solutions or numerical finite element models, have predominantly approximated the overriding or upper crust as a mechanically homogeneous elastic medium by neglecting variable earth structure (*10*) and delegating structural complexity to kinematic corrections rather than varying elastic moduli. Even viscoelastic formulations that incorporate mantle or glacial-isostatic relaxation generally assume a purely elastic, laterally invariant continental plate (*8*, *11*). Yet along-strike

variations in upper-plate stiffness of tens of gigapascals are mechanically significant, as they alter the partitioning of interseismic strain and can bias geodetically inferred coupling patterns even when fault-slip conditions are identical (*12*). Numerical experiments further demonstrate that neglecting variable rigidity can introduce significant distortions (often up to 50%) in calculated surface deformation and subsurface shear-stress estimates, especially in thrust-faulting regimes (*13*). Thus, ignoring upper-crustal heterogeneity risks conflating mechanical contrasts in the overriding plate with true variations in megathrust frictional state.

Beyond its influence on elastic strain partitioning, upper-crustal composition actively modulates megathrust mechanics through vertical loading, effective normal stress, and rheological segmentation. Density contrasts within the forearc directly affect lithostatic pressure on the plate interface, with dense mafic crust promoting stronger coupling and lower-density crust favoring aseismic slip (*14*). Observations from multiple subduction zones show that along-strike variations in interseismic coupling and slow-slip recurrence often coincide with forearc structural transitions rather than slab geometry alone (*15–17*). At smaller scales, gradients in fluid pressure, permeability, and the distribution of strong blocks within weak, hydrated matrices further localize deformation and regulate rupture propagation (*16–18*). Together, these lines of evidence indicate that upper-crustal strength is not merely a boundary condition imposed on subduction systems, but an active control on stress accumulation, slip behavior, and mechanical segmentation along the plate interface.

Forearc geology, such as contrasts in crustal density, composition, thickness, and fluids, imposes mechanical segmentation that may govern stress transfer across the plate interface. For instance, density-driven variations in vertical loading have been evidenced to modulate megathrust shear strength (*14*). Also, geodetic analyses show that mechanically weak segments may act as rupture barriers, which demonstrates that segmentation is imposed by upper plate structure rather than by transient seismic cycle effects (*15*). Over longer timescales, upper crustal strength contrasts may regulate forearc deformation and orogenic development by controlling where both elastic and permanent strain is stored versus distributed (*19–21*). These same strength contrasts also determine whether deformation remains localized on the megathrust or is partitioned into the upper plate, with strain partitioning emerging only where inherited crustal weaknesses permit stress transfer (*22*). Therefore, accounting for along-strike upper-crustal heterogeneity is essential for interpreting interseismic deformation at Cascadia and for improving physical models of megathrust behavior.

To evaluate the hypothesis that upper-crustal geology modulates interseismic deformation, we examine the central segment of the CSZ (42°–44.5° N) in central-to-southern Oregon (**Fig. 1**). This region represents the margin's most tectonically heterogeneous sector (*5*, *6*), reflecting episodic accretion of distinct terranes during a complex history of long-lived subduction and continental lithospheric growth (*23*). At approximately 43.5° N, the forearc undergoes a major lithological shift where the overriding plate transitions abruptly along strike from the Franciscan and Klamath terranes in the south to the Siletz terrane in the north. This terrane-scale juxtaposition creates sudden lateral contrasts in lithology (**Fig. 1b**), crustal thickness (*24*, *25*), vertical load (*5*), and inferred mechanical strength (*6*) that remain poorly resolved (*5*).

To the north, the upper plate is underpinned by the Siletz terrane (**Fig. 1a**), a Paleocene–Eocene large igneous province that accreted rapidly to North America (*26*). Composed of thick, plateau-derived basalts, it forms a robust, seaward-dipping backstop (*24*, *26*). In contrast, the nearshore southern section is dominated by the Jurassic–Cretaceous Central

Belt of the Franciscan terrane (*23*, *27*). Consisting predominantly of clastic sedimentary rocks and mélanges with subordinate metamorphic and mafic components, it records prolonged accretion and deformation within the subduction complex (*27*, *28*). Inland, this weaker, sediment-dominated assemblage gives way to the Klamath terrane, an amalgamated collage of oceanic crust, arc volcanics, mélanges, and ophiolites stitched together by plutonic intrusions (*29*). These sudden along-strike changes in upper-crustal composition and rigidity, reinforced by fault-bounded terrane contacts, spatially correlate with distinct variations in geophysical observations that act as proxies for subduction mechanics (**Fig. 1c**). Specifically, the southern termination of the rigid Siletz block demarcates a zone where interseismic uplift rates increase from negligible in the north to >2 mm/year in the south (*30*), and tremor density intensifies (*31*) with shorter Episodic Tremor and Slip (ETS) recurrence intervals (*4*). Furthermore, these upper-crustal terrane boundaries coincide with a significant along-strike change in slab curvature, specifically a distinct shallowing south of the Siletz terrane (*5*, *32*).

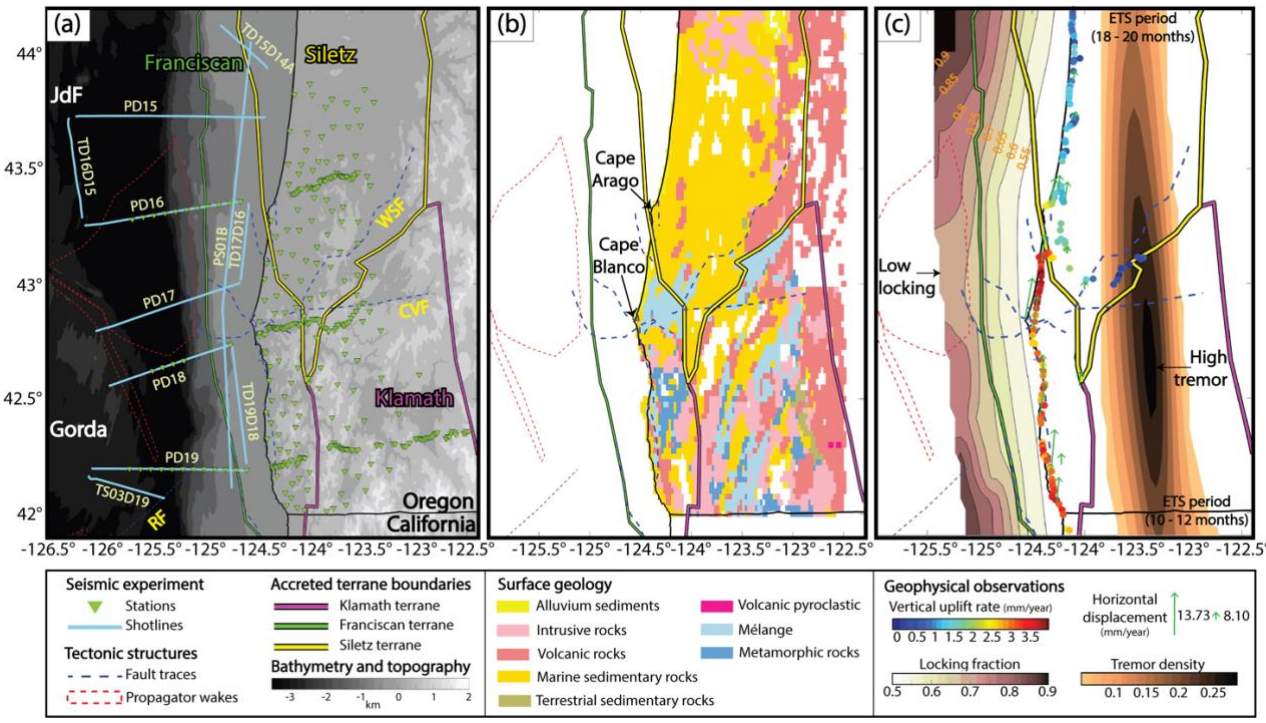

Figure 1: Geological framework and geophysical observations of the south-central Cascadia Subduction Zone. (A) Map of seismic stations and shot locations from central to southern Oregon used to develop the shore-crossing 3-D seismic velocity model. Major tectonic features are shown, including fault traces and oceanic propagator wakes. The Canyonville Fault (CVF) and Wildlife Safari Fault (WSF) are drawn from (*33*); the Rogue Fault (RF) is from (*34*), and additional fault traces are from the U.S. National Seismic Hazard Model 2023 (*35*). Boundaries of the three accreted terranes from (*28*) are also shown. **(B)** Surface geology of the study area from the Oregon Department of Geology and Mineral Industries (*36*). **(C)** Geophysical observations across the study region highlighting differences between the northern and southern parts of the south-central CSZ, including uplift rates in circles (*30*), locking fraction (*8*), and episodic tremor and slip (ETS) periods (*4*).

The influence of upper crustal segmentation of strength on the subducting plate interface and its mechanical behavior at subduction zones remains to be fully resolved by direct observations (*4*). Therefore, our first goal is to characterize the detailed nearshore crustal structures by developing a 3-D high-resolution shore-crossing P-wave seismic velocity (Vp) model through the joint inversion of active-source P and PmP arrivals (see **Figs. 1a** and **S1** for experiment setup). This model resolves the shallow (0–20 km) architecture of accreted terranes and major faults while also capturing the geometry of the subducting

oceanic slab. We spatially link these structural constraints on upper-crustal heterogeneity to the along-strike slab bending and interseismic coastal uplift rate. Second, we quantify the mechanical controls by converting tomographic velocities into density and elastic moduli to drive numerical simulations. Integrating 1-D finite-difference slab flexure modeling with a viscoelastic kinematic framework, we assess the extent to which seismically derived backstop rigidity influences subduction zone geometry and coastal uplift. The correspondence between these rigidity-driven simulations and observational data serves to validate the governing role of upper-crustal structure in subduction dynamics.

RESULTS

Vp tomographic inversion

We modeled the shallow crustal structure (0 – 20 km) and slab Moho depth around offshore and onshore southern Oregon (42°N – 44°N) using a joint inversion of P and PmP arrivals (see **Materials and Methods** section for details). Supported by dense ray coverage and high derivative weight sum (DWS) values (**Fig. S2**), our modeling results in a robust (RMS misfit of 68.4 ms; **Fig. S3**), high-resolution model that effectively resolves 5 – 10 km scale tectonic heterogeneities and sharp along-strike contrasts (see supplementary **Text S1** and **Fig. S4** for checkerboard test result).

Four primary components are readily identified in our tomographic model: the sedimentary accretionary prism, the accreted upper-crustal terranes, the subducting oceanic slab, and the underlying upper mantle (**Figs. 2** and **3**). The accretionary prism is characterized by the lowest velocities, with Vp values of ~3–5 km/s, reflecting its weak, sediment-dominated composition. Beneath the prism, the subducting slab exhibits Vp values of ~6.0–6.5 km/s west of the deformation front (trenchward), decreasing to ~5.0–6.5 km/s directly beneath the prism. At greater depths, the upper mantle is distinguished by significantly higher velocities, generally ranging from ~7.5 to 8.2 km/s. Together, these contrasts set the context and provide a framework for examining lateral variations within the upper crust and slab topography.

The tomographic model reveals pronounced along-strike velocity differences among the individual overlying terranes (**Figs. 2, 3, S5,** and **S6**). The Franciscan exhibits the lowest velocities and greatest variability. In this study, we divide the Franciscan terrane into its offshore and onshore parts because of their high Vp contrast (**Fig. 2a**). Vp ranges mostly from 3.0-5.5 km/s (mean: 3.4-4.75 km/s; **Fig 2b**) for offshore Franciscan and from 4.0-6.0 km/s (mean: 4.5-5.7 km/s) for onshore Franciscan. In contrast, the Klamath unit displays the highest velocities and least variability, characterized by Vp values mostly between 5.5–6.5 km/s (mean: 5.75-6.2 km/s). The Siletz terrane is intermediate, with Vp ranging between 4.5-6.5 km/s (mean: 5.0-5.9 km/s). The Vp structures of the accreted terranes align well with Bouguer gravity anomalies (**Fig. 2d**), lending confidence to the robustness of our results.

Our results also show intra-terrane Vp fluctuations that are driven by both inherent lithological diversity of each terrane (*38*, *39*) and localized deformation structures such as faults (*33*). The presence of faults is notable in the southernmost extent of the Siletz terrane, where multiple crustal fault strands dissect through all terranes (**Fig. 1a**). These fault zones, concentrated between 42.75°N and 43.35°N latitude, exhibit localized velocity reductions (~1.0 km/s) relative to the surrounding crust. While these low-Vp anomalies are most pronounced at depths < 5 km, they persist even to depths of 15 km (**Fig. 2a**). Our tomographic results reflect a distinct three-way latitudinal division of the onshore terranes that may influence subduction mechanics. North of 43.5°N, the Siletz terrane exhibits a

relatively coherent Vp structure with velocities typically ranging from 5.0 to 6.5 km/s. In contrast, the highly faulted region between 42.75°N and 43.35°N shows the lowest Vp, ranging from 4.0 to 5.5 km/s. South of 42.75°N, the onshore Franciscan terrane is characterized by a Vp range of 4.5–6.0 km/s, representing a velocity regime lower than the coherent northern Siletz block but higher than the heavily faulted central zone.

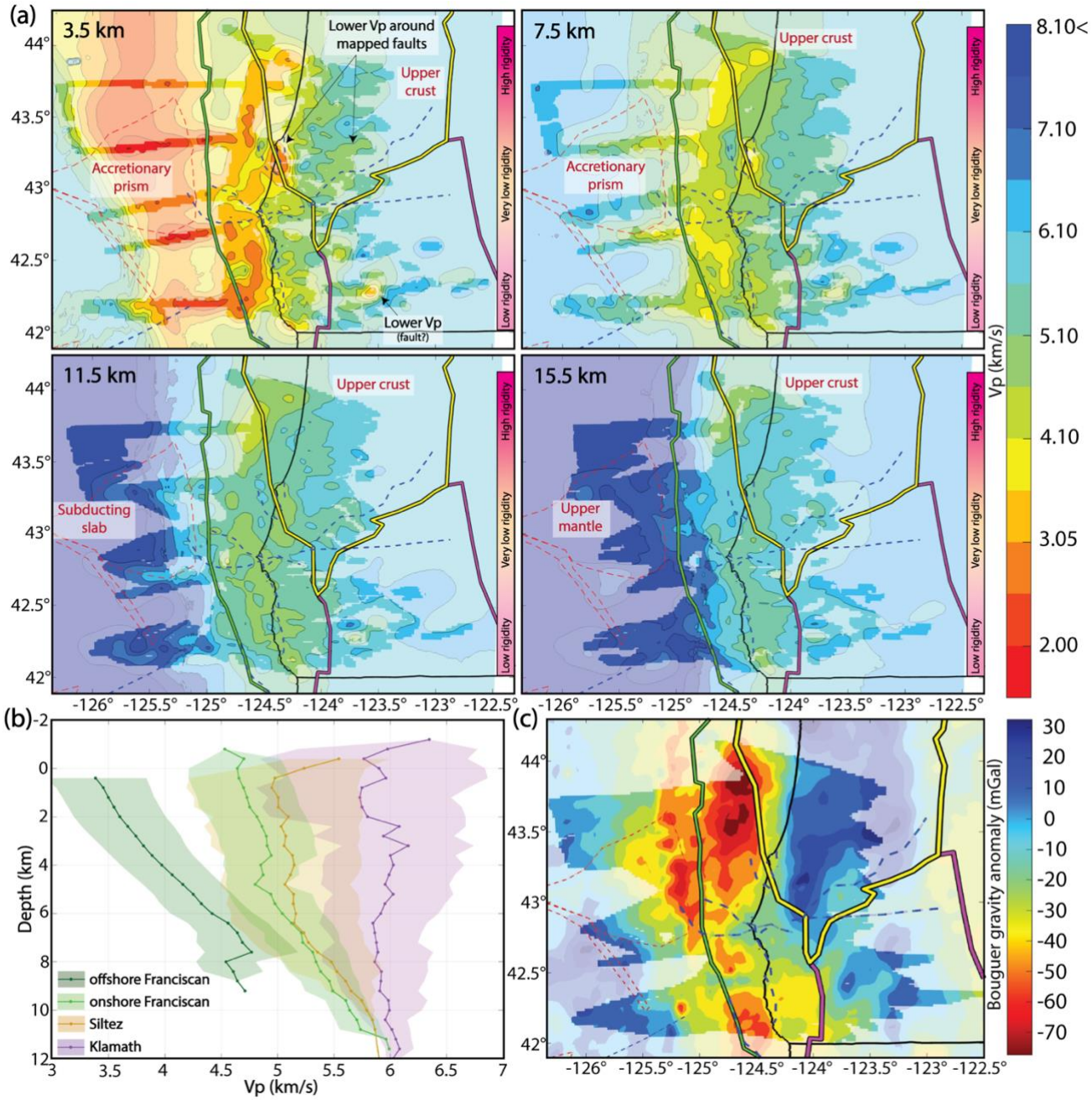

Figure 2: 3-D velocity structure and gravity anomaly of the south-central CSZ. (A) Map sections of the high-resolution 3-D Vp tomographic model at selected depth intervals. Dark-toned regions indicate areas with seismic ray coverage (DWS>10; **Fig. S2**), while light-toned regions represent unsampled volumes. Tectonic features are shown with the same symbols as in **Figure 1**. See **Figure S2** in the supplementary material for map sections every 2 km. **(B)** Average Vp-depth profiles for the accreted terranes in the study area. Solid lines show mean Vp trends, small circles mark sampling depths from the 3-D model, and shaded envelopes indicate standard deviation. **(C)** Bouguer gravity anomaly map from the USGS online repository (*37*).

These findings highlight two primary modes of velocity distribution: terrane-specific averages reflecting bulk lithological properties, and along-strike fluctuations that transcend terrane boundaries due to localized deformation. We emphasize that these subsurface Vp distributions can be reliably estimated by integrating surface geology with established regional tectonic frameworks. For instance, while the northern and central Siletz regions are largely obscured by recent alluvial deposits (**Figs. 1b** and **S7**), regional geological constraints can predict a basaltic lithology (*26*, *39*) with Vp between 5.5–6.5 km/s for the unfractured northern block (*40*) and at least a 0.5–1.0 km/s velocity reduction within the highly faulted central regime (*41*). Farther south, Vp estimates based on surface geology for the onshore Franciscan and Klamath terranes closely align with our modeled Vp distributions (**Fig. S7b**), demonstrating that surface mapping can be a powerful proxy for characterizing upper-crustal structures.

While our overall Vp distribution is consistent with large-scale low-resolution terrane boundaries, which are mostly inferred from potential field data (*24*, *28*), our high-resolution model can map the boundaries at a finer scale. To better constrain the boundaries, we generate terrane-specific similarity maps (**Fig. S8**) by comparing every 1-D Vp depth profile of the tomographic model against the terrane-averaged Vp depth profile (**Fig. 2b**). This analysis allows us to delineate the western boundary of the onshore terranes on a scale of 3-5 km resolution (**Fig. 4**). We also calculate the terrane-specific similarity index for the full 3-D tomographic volume, and using the 90% similarity contour (**Fig. S8**) for every depth interval, we extract the 3-D western or seaward boundary of the onshore accreted terranes. In **Figure 5**, we show this refined 3-D boundary of Siletz and onshore Franciscan as they form the shoreline-adjacent upper crustal terrane backstop in our study area. We identify a consistent seaward-dipping backstop that varies in geometry along strike. North of 43.3°N, the intact high-Vp Siletz block forms a gently dipping backstop (30°–40°). South of 43.3°N, however, the boundary steepens significantly (60°–80°) both adjacent to the lower-velocity faulted Siletz region, and along the onshore Franciscan terrane that dominates the nearshore regime south of 42.9°N.

Inversion of PmP arrivals yields a high-resolution 3-D structure of the nearshore Moho interface (**Fig. 4**). The data provide a sampling density averaging 5–10 ray hits per km^2. In the northern region (near 42.8°N), the modeled Moho beneath the Siletz terrane ranges in depth from ~22.5 to 30 km. To the south (near 42.2°N), the Moho beneath the Franciscan terrane ranges from ~17.5 to 20 km. Between 43°N and 43.6°N, the western boundary of the Siletz terrane extends seaward before retreating landward; Moho depth contours in this region deepen beneath the seaward extent and shallow under the landward retreat. Additionally, shallower Moho depths are observed to the southwest at latitudes corresponding to onshore upper-crustal faults.

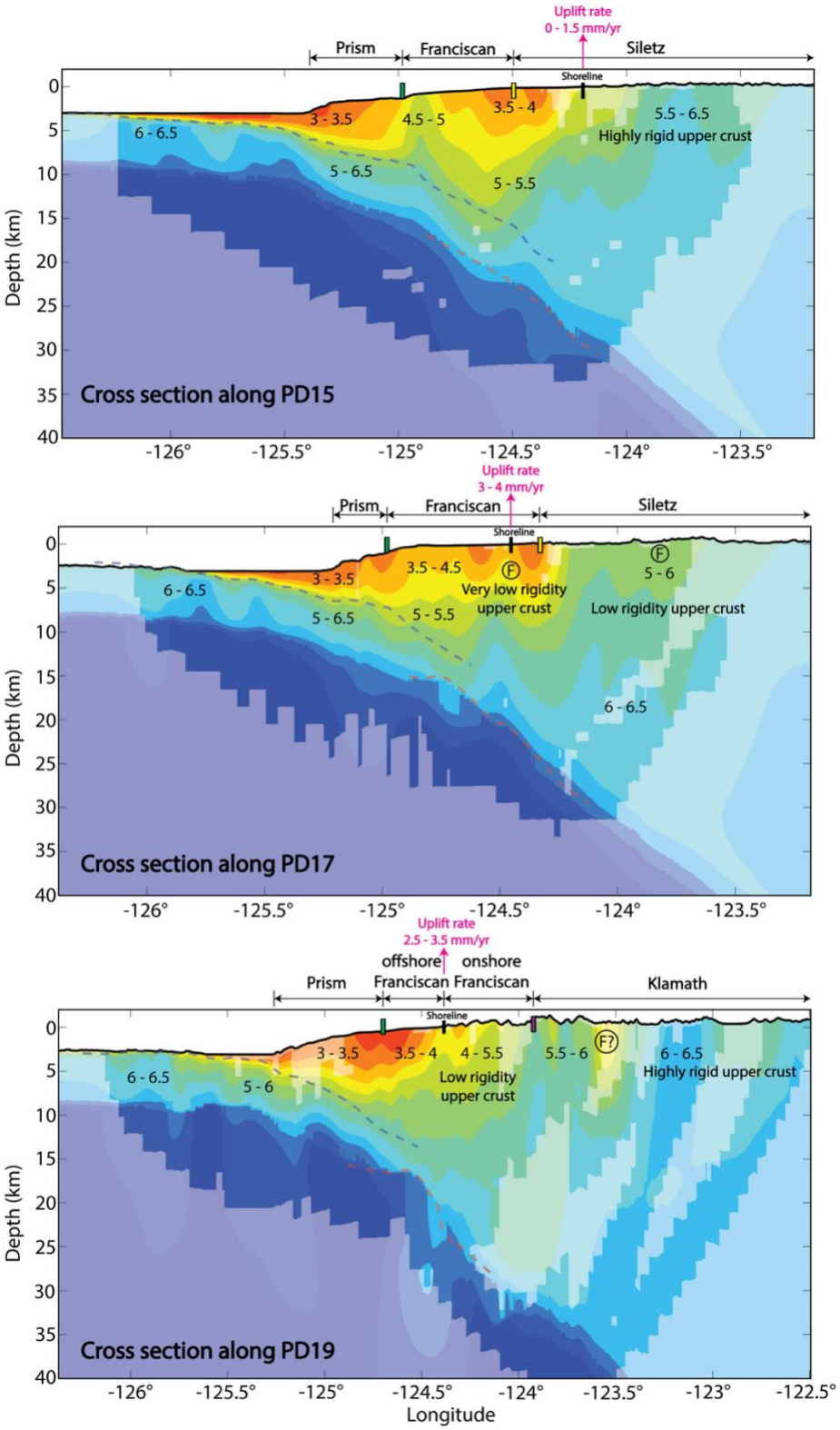

Figure 3: Across-strike cross sections of the 3-D shore-crossing Vp model of the CSZ. Profiles follow offshore seismic shotlines and onshore dense nodal lines in the northern (PD15), central (PD17), and southern (PD19) study area. Colors and labeled contours indicate Vp values (km/s) using the same color scale as **Fig. 2**. Major tectonic boundaries, such as the accretionary prism, accreted terranes, shorelines, and known and inferred faults (F) are indicated along the top of each section. Observed coastal uplift rates from (*30*) are also shown on each profile. The blue dashed lines show the slab top from (*32*) and the red dashed lines show slab Moho from our PmP inversion results (**Fig. 4**). Inferred relative changes in upper crustal rigidity based on the along-strike seismic velocity changes are labelled.

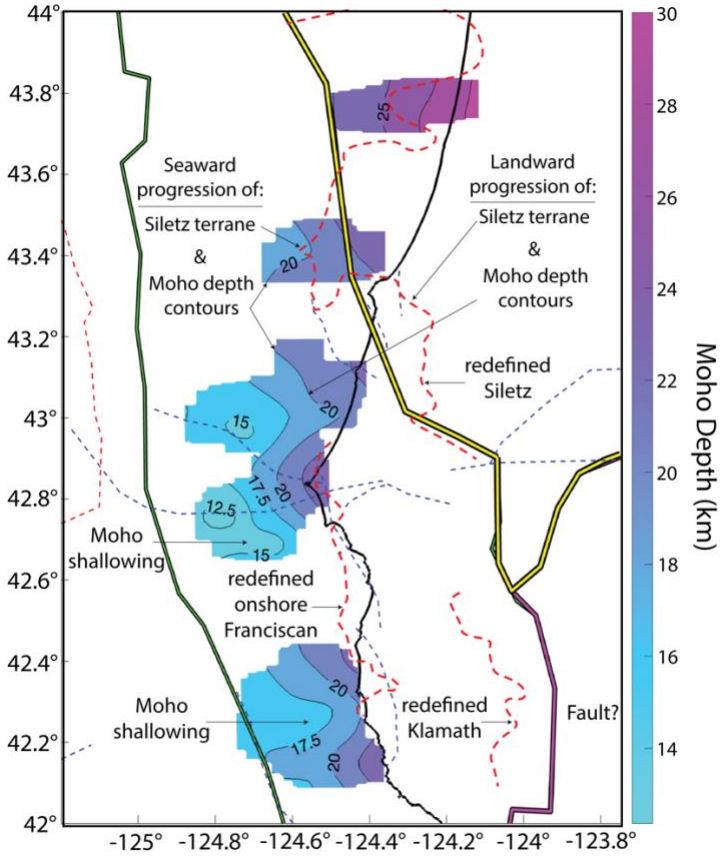

Figure 4: Color-filled contours of Moho depth from the inversion, shown only where PmP reflections sample the interface. Tectonic features (terrane boundary, faults, and propagator wakes) follow the symbology in **Fig. 1**. Red dashed lines mark the redefined western boundaries of the onshore terranes, inferred where our similarity analysis shows 90% similarity to the average Vp-depth profile of each terrane (**Fig. 2b**).

Correlation of Vp structure with indicators of subduction mechanics

In the south-central CSZ, the forearc transitions from the Siletz terrane in north, composed of thick intrusive and volcanic rocks, to the Franciscan and Klamath terranes in south, dominated by clastic sediments, mélanges, and amalgamated oceanic and volcanic arc assemblages (**Fig. 1b**). These lithological contrasts manifest as distinct variations in crustal density and, consequently, the along-strike Vp structure of the overriding plate (**Figs. 2** & **3**). Here, we demonstrate how this heterogeneous upper-crustal Vp structure directly correlates with multiple independent indicators of mechanical segmentation, specifically subducted plate topography, coastal uplift rates, onshore relief, and upper-crustal backstop geometry.

First, we observe a correlation between along-strike variations in upper-crustal Vp and Moho depth. Broadly, the Moho is deeper beneath the high-velocity Siletz terrane and shallower beneath the lower-velocity faulted Siletz and onshore Franciscan terrane (**Figs. 4**, **5**, **6,** and **7**). North of 43.25°N, the Moho deepens beneath the thickened Siletz block. South of this latitude, where the Siletz terrane retreats landward to be replaced by the Franciscan and Klamath terranes, crustal faults complicate the velocity structure; notably, low-Vp zones associated with the WSF and CVF coincide with localized Moho shallowing. This correlation persists at finer scales, where Moho depth contours closely track the seaward and landward extent of the high-Vp Siletz terrane (**Fig. 4**).

Furthermore, the modeled along-strike variation in upper-crustal Vp correlates strongly with coastal uplift rates, exhibiting a distinct inverse relationship (**Figs. 3**, **5**, and **6**). North of 43.25°N, high Vp within the Siletz terrane corresponds to relatively low uplift rates (0.5–2 mm/yr). Conversely, south of 43.25°N, a sharp decrease in nearshore Vp, associated with the faulted Siletz and Franciscan assemblages, coincides with an abrupt increase in uplift to 2.5–3 mm/yr. This inverse pattern persists southward: a local increase in Vp near 42.75°N aligns with a modest decline in uplift, while the return to low Vp south of ~42.4°N is matched by higher uplift rates.

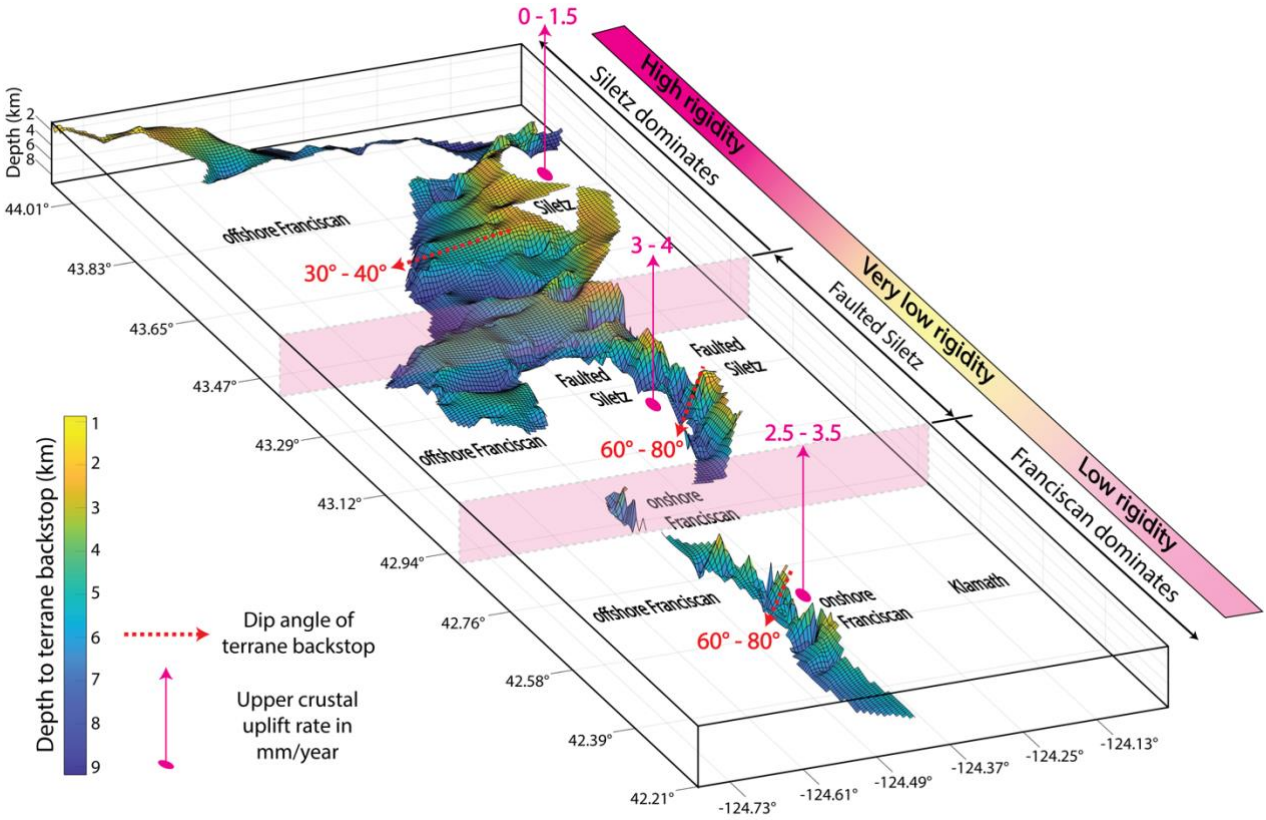

Figure 5: 3-D geometry of the western boundary of the nearshore terranes (Siletz in the north and Onshore Franciscan in the south) from the similarity index calculation through the entire model volume (see **Materials and Methods** and **Fig. S8** for more details).

Topography provides an additional, independent surface expression of this mechanical segmentation. Across the along-strike transition from the high-Vp Siletz terrane to the low-Vp onshore Franciscan terrane, the maximum onshore relief increases markedly: peak elevations in the Siletz-dominated segment are ~0.6-0.8 km lower than in the Franciscan segment (**Figs. 1a and S9**). This first-order topographic step is spatially coincident with the shift to lower Vp and higher coastal uplift rates, consistent with stronger interseismic shortening and long-term vertical growth in the lower-Vp forearc.

A correlation also exists between the backstop angle of nearshore terranes and the Vp of the nearshore upper crust. 3D mapping of these boundaries (**Fig. 5**) reveals that the high Vp Siletz terrane exhibits a gently dipping backstop (30°-40°). In contrast, the lower Vp onshore Franciscan terrane is characterized by a significantly steeper backstop (60°-80°).

The observed correlations between Vp structure and various mechanical indicators suggest that segmentation in upper crustal density and rigidity drives subduction dynamics. Based on these observations, we subdivide the south-central CSZ upper crust into three mechanical domains (**Fig. 6**). In the north, the intact, high-Vp Siletz terrane correlates

with a deeper Moho and minimal uplift, defining a high-rigidity domain. Central to the study area, the heavily faulted Siletz transitional zone exhibits the lowest Vp values, a shallow Moho, and peak uplift rates, forming a very low-rigidity domain. Further south, the nearshore Franciscan assemblage displays moderate Vp, a shallow Moho, and high uplift, representing a low-rigidity domain.

Conceptual model for subduction mechanics

To test the hypothesis that upper-plate strength controls nearshore subduction mechanics, we conceptualize a numerical model varying only crustal properties reflecting density and rigidity to predict slab topography and onshore uplift (**Fig. 8**). First, we show that high-density blocks impose a greater vertical lithostatic load, effectively pushing the slab to greater depths compared to the lower-density blocks (*42*, *43*). Secondly, our results indicate that upper-plate rigidity modulates the mechanical response to interseismic horizontal shortening, creating distinct coastal uplift patterns between high- and low-rigidity terranes.

Regarding the first mechanism, we observe that peak slab undulation spatially correlates with the seaward terminus of the onshore terranes (**Fig. 7**), indicating maximum flexural response at the primary across-strike Vp gradient. This flexure is likely a loading-dominated response, as downward deflection begins seaward of the terrane edge alongside localized Vp reductions (**Fig. 3**) indicative of bending-fault hydration (*44*, *45*).

Secondly, the structural integrity of the overlying terrane controls the resulting strain distribution and uplift. Interseismic uplift reflects a superposition of recoverable elastic strain accumulation and permanent plastic deformation (*6*, *21*, *46*). At this late stage of the megathrust cycle in CSZ, elasto-plastic loading dominates over mantle relaxation as the primary driver of vertical motion (*21*). While seismically derived elastic moduli constrain the recoverable strain component, the magnitude of permanent deformation depends on the rheological competency (*6*) and geometry of the backstop (*46*). The high-rigidity Siletz backstop limits landward stress transfer, and its gently dipping geometry forces strain to localize offshore, resulting in minimal coastal uplift. In contrast, the low-rigidity Franciscan backstop has a lower yield strength, allowing efficient landward stress propagation. This facilitates permanent internal shortening and a steeper deformable backstop, manifesting as the significantly higher coastal uplift rates observed geodetically. Ultimately, the rheological contrast between the offshore wedge and the onshore backstop acts as the primary mechanical filter converting plate convergence into upper crustal vertical growth.

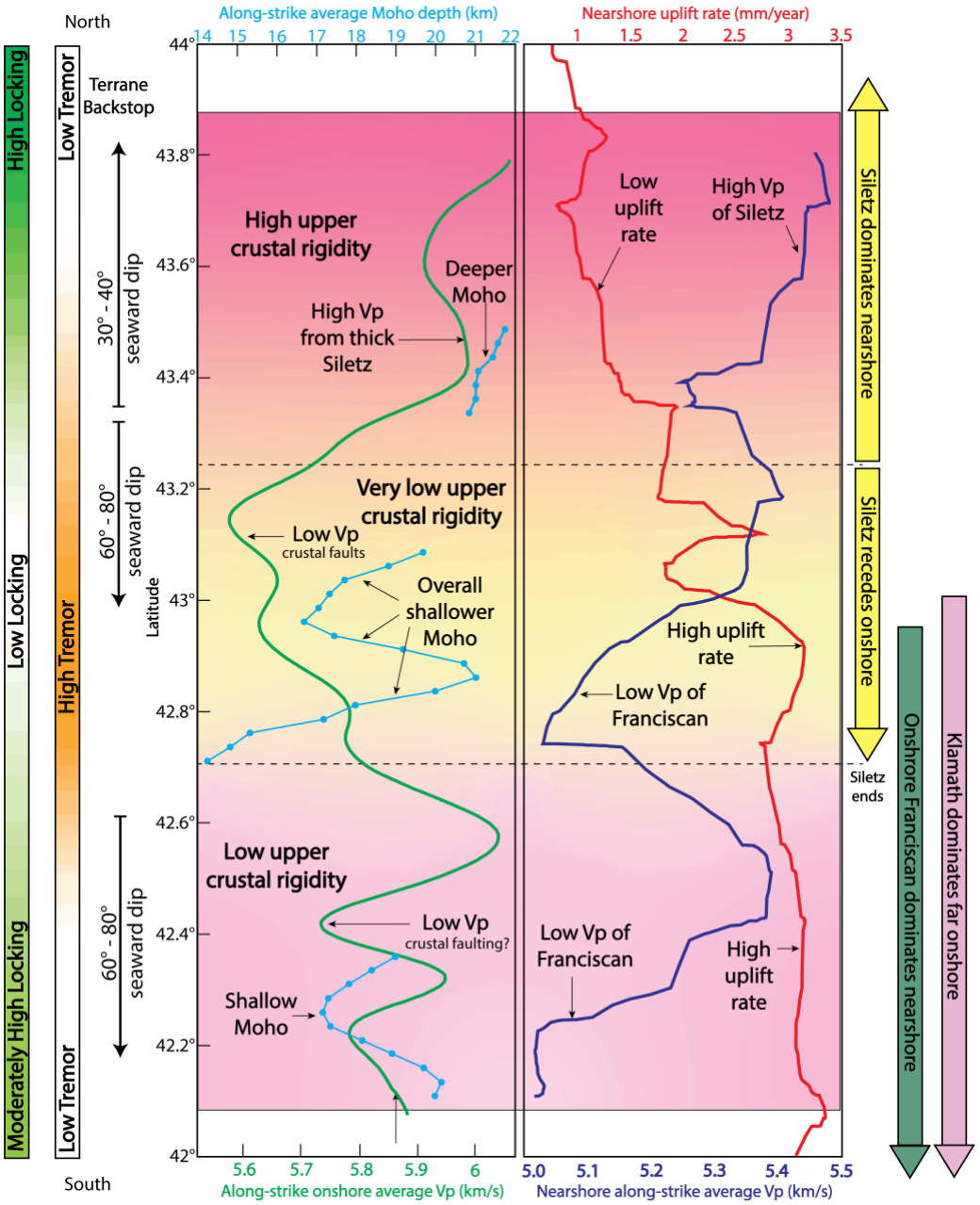

Figure 6: Different trends showing correlation between geologic/tectonic features and geophysical observations along-strike of the subducting slab, highlighting their north-south variations. Left panel: average onshore Vp at 9 km depth (green), calculated by averaging onshore values within each latitude interval of the tomographic model and applying a Gaussian mean smoothing. Also shown is the along-strike Moho depth averaged within latitudinal intervals. Right panel: uplift rate along shoreline from (*30*) (red), averaged within each latitude interval, and then compared with nearshore average Vp (blue). The nearshore Vp values were computed from 7 – 9 km depth at uplift rate measurement sites and smoothed using a Gaussian mean across latitude intervals. See **Fig. S10** in the supplementary material for the calculation of the Gaussian smoothed mean.

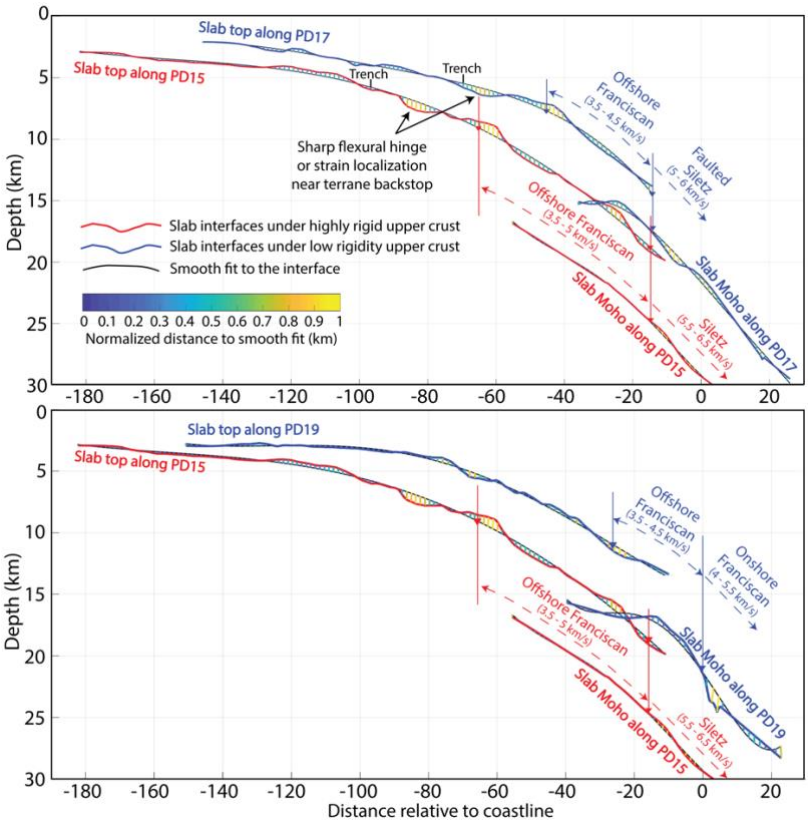

Figure 7: Depth profiles of the top and bottom of the subducting slab along offshore seismic shotlines. The profiles are shown for the northern high-rigidity segment (PD15; red) and southern low-rigidity segments (PD17 and PD19; blue). Profiles are plotted as depth versus distance relative to the coastline, with negative values offshore and positive values onshore. Solid colored curves mark the interpreted slab top and bottom (or Moho) along each profile, while black curves show a smooth reference fit to the interface used to quantify deviations in slab geometry. Color shading along the slab interfaces denotes the normalized distance to the smooth fit (0 - 1), highlighting zones of localized curvature and departures from long-wavelength bending. Boundaries of upper crustal features (trench and terranes) are indicated along the profiles.

Numerical simulation of subduction mechanics

To test whether along-strike variations in upper-crustal rigidity are sufficient to explain the observed segmentation in slab geometry and coastal uplift, we conducted forward mechanical simulations constrained by our tomographic velocity structure (**Fig. 9**). We converted seismic velocities into density and elastic moduli, evaluating the high-rigidity Siletz and lower-rigidity Franciscan endmembers while holding all other subduction parameters (convergence rate, slab age, mantle density, and far-field boundary conditions such as slab pull) constant. To account for velocity uncertainties, we employed a stochastic Monte Carlo approach (see **Materials and Methods** for details).

First, we tested the effect of upper-plate density (which scales directly with Vp) on nearshore slab geometry using a 1-D finite-difference flexural model. The simulations show that this difference in vertical loading alone deflects the slab approximately 2 km deeper (average of all Monte-Carlo realizations) beneath the high-density Siletz terrane compared to the lower-density Franciscan terrane (**Fig. 9**). This matches the magnitude and spatial pattern of our observed Moho depths (**Figs. 4, 5,** and **6**), confirming that upper-plate density contrasts mechanically reproduce the along-strike segmentation in slab bending without invoking changes in slab buoyancy or plate kinematics.

Next, we evaluated interseismic coastal uplift using a kinematic viscoelastic formulation to capture both instantaneous elastic strain accumulation and time-dependent viscous deformation (*6*, *21*, *46*, *47*). A purely elastic simulation produced only a modest uplift contrast between terranes (~0.3 mm/yr, or ~20% of the observed difference) (**Fig. 9**). In contrast, incorporating viscoelastic strain partitioning fully reproduced the observed ~2 mm/yr uplift contrast. Achieving this required a difference in Maxwell relaxation times: ~250 years for the compliant Franciscan terrane versus ~50,000 years for the rigid Siletz terrane.

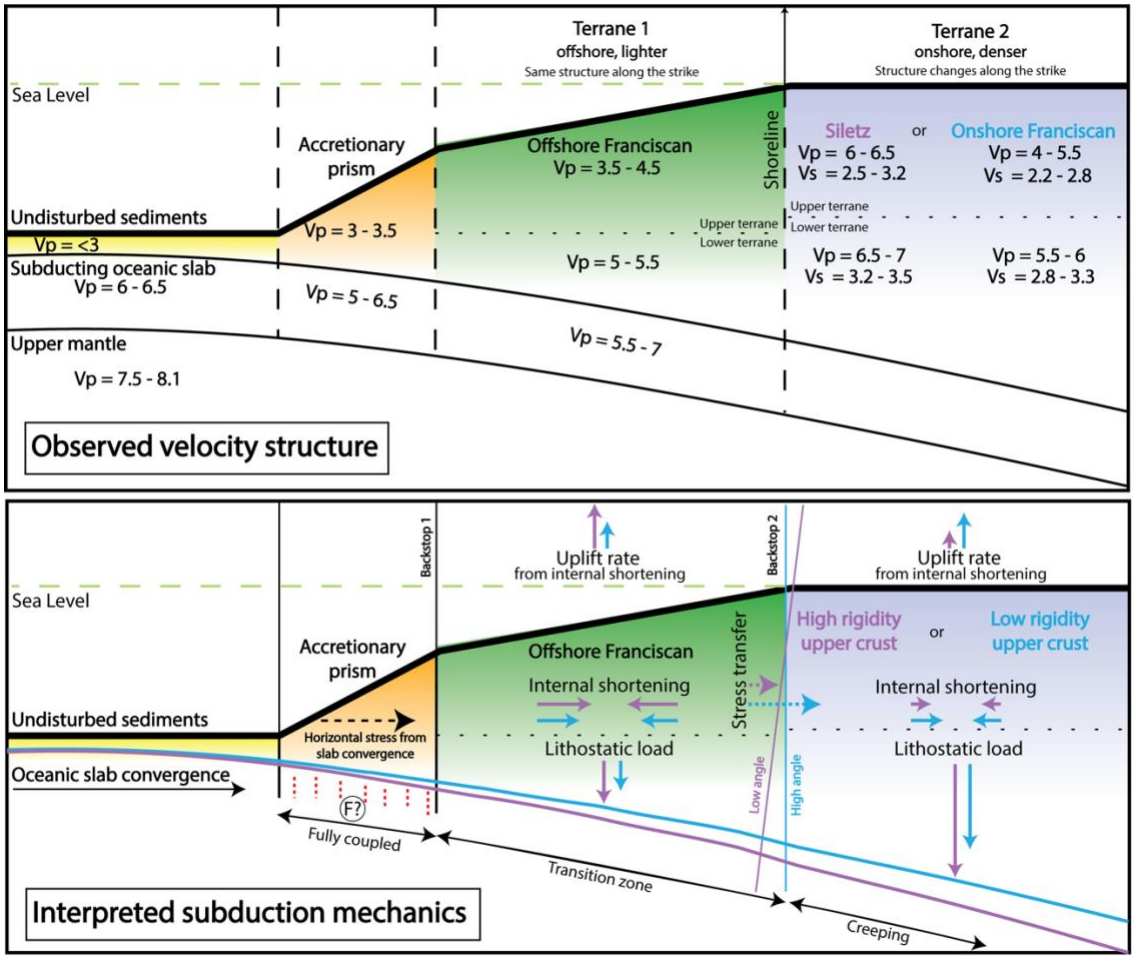

Figure 8: Conceptual model linking observed seismic velocity structure to along-strike variations in subduction mechanics. Top section shows an idealized across-strike cross-section illustrating the seismic velocity structure resolved by the shore-crossing tomography. Shaded regions indicate major tectonic units, including the accretionary prism, offshore Franciscan (Terrane 1), and onshore terranes (Terrane 2), with representative Vp and Vs ranges annotated for each unit. The onshore domain includes either high-velocity Siletz crust or lower-velocity onshore Franciscan crust, and upper–lower terrane subdivisions are indicated by dashed lines. Bottom section shows the corresponding schematic of the mechanical elements inferred from tomographic results and considered in the analysis. They include convergence direction, slab interface, lithostatic loading, internal shortening within forearc terranes, stress transfer across the backstop, backstop geometry, and uplift resulting from internal shortening. Arrows denote directions of either stress transfer between terranes or the rate of shortening and vertical motion.

This result shows that in the high-rigidity scenario, the backstop acts as a mechanically rigid buttress that resists internal deformation (0 mm/yr uplift), forcing strain to localize within the weaker offshore wedge. Conversely, in the low-rigidity scenario, the onshore backstop is compliant enough to absorb tectonic stress through distributed internal shortening, driving significant nearshore uplift (~1.8 mm/yr). Together, the numerical

simulations (**Fig. 9**) confirm that upper-crustal rigidity controls subduction mechanics through two complementary pathways: density contrasts impose variable vertical loads that modulate slab bending, while rigidity-dependent rheology governs how interseismic shortening is partitioned, controlling the amplitude of coastal uplift.

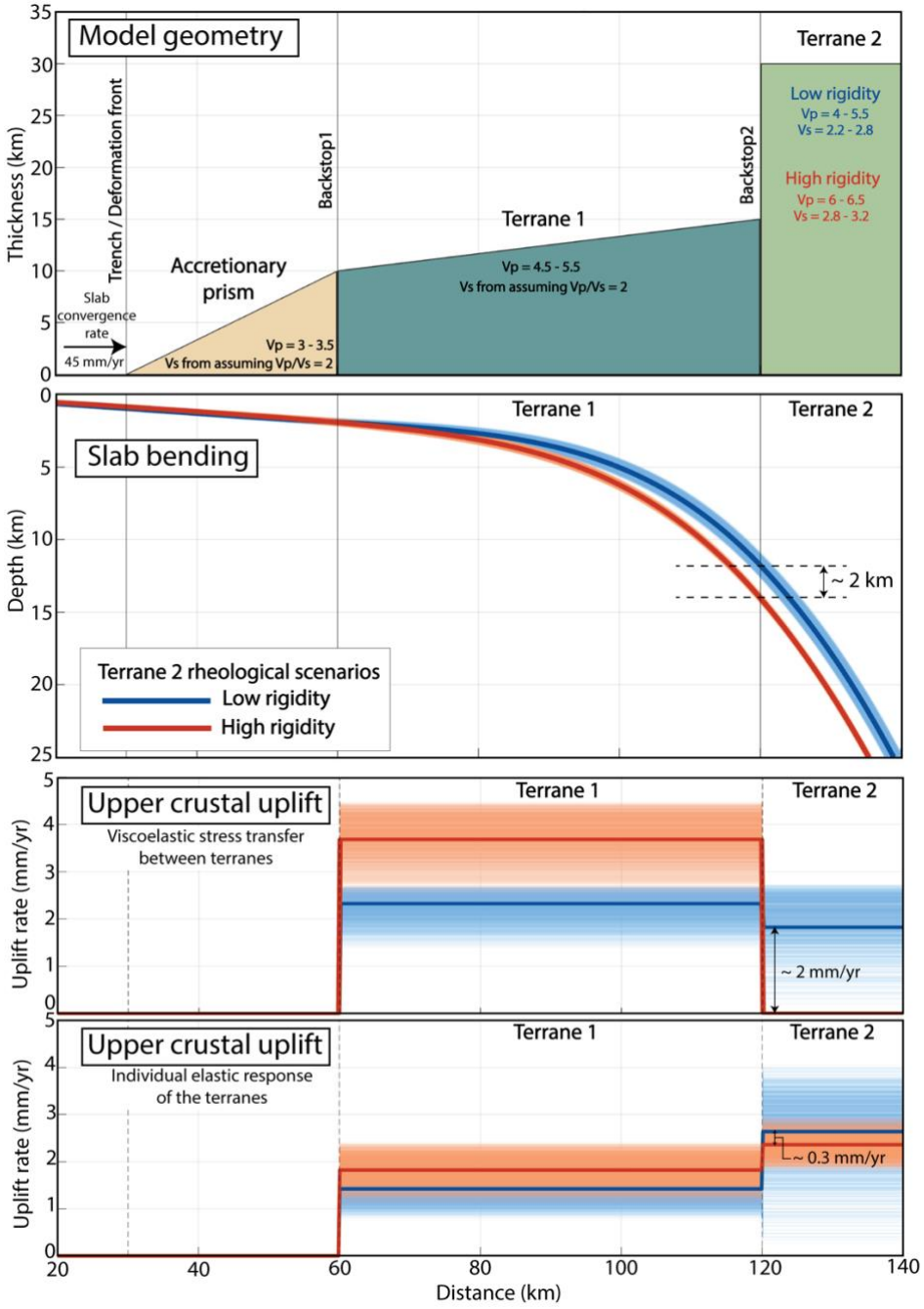

Figure 9: Numerical simulation setup and modeled responses for slab bending and upper-crustal uplift. The top panel shows the model geometry used in the numerical experiments. The forearc is divided into an accretionary prism, Terrane 1 (offshore forearc), and Terrane 2 (onshore forearc), separated by idealized backstops. Representative Vp and Vs ranges assigned to each unit are shown, with Vs inferred assuming Vp/Vs = 2 where noted. Slab convergence rate and trench/deformation front location are indicated. The second panel shows modeled slab bending beneath Terrane 1 and Terrane 2 for two rheological end-member scenarios assigned to Terrane 2: low rigidity (blue) and high rigidity (red). The third panel shows modeled upper-crustal uplift rates that include viscoelastic stress transfer between terranes. The bottom panel illustrates upper-crustal uplift rates predicted from the individual elastic response of each terrane, without viscoelastic stress transfer. Solid lines show the mean result, with shaded envelopes representing the spread of Monte Carlo realizations.

DISCUSSION

Impact of upper crustal heterogeneity on subduction mechanics

Our tomographic model (**Figs. 2 and 3**) resolves a forearc whose mechanical architecture is set by inherited lithology, fault damage, and fluid distribution rather than by depth alone, consistent with along-strike segmentation documented at other convergent margins (*19*, *20*). The geologically heterogeneous south-central CSZ forearc exemplifies this process (*4*, *48*). Three domains emerge: a coherent high-Vp Siletz block, a faulted low-Vp transitional zone, and a moderate-Vp onshore Franciscan segment (**Figs. 2a** and **6**). Each domain exhibits a distinct backstop geometry (**Figs. 4** and **5**), ranging from a gently dipping rigid buttress (30°–40°) in the north to steep, deformable boundaries (60°–80°) in the south, mirroring the static-versus-dynamic backstop distinction documented in other accretionary systems (*28*, *50*). The terrane-scale Vp hierarchy (**Fig. 2b**) is independently corroborated by surface geology (**Fig. 1b**) through empirical velocity–lithology relationships (*40*, *49*) and supported by Bouguer gravity (**Figs. 2c** and **S7**), together providing the mechanical framework for interpreting along-strike variations in subduction dynamics.

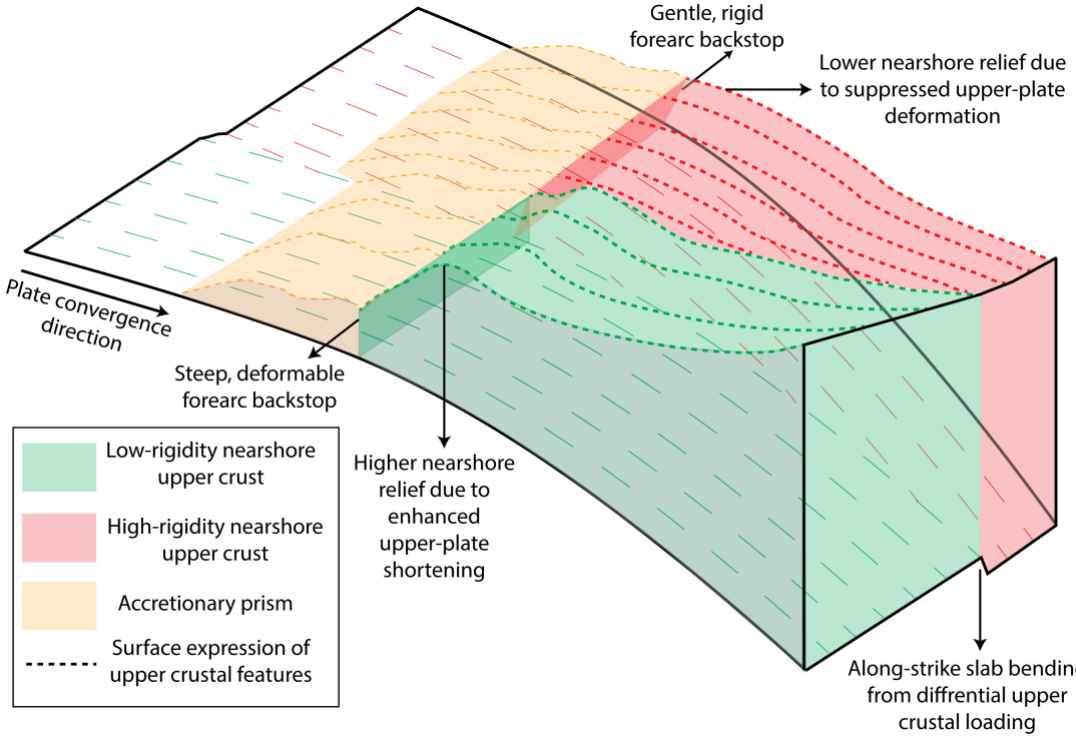

Figure 10: Conceptual 3-D model illustrating the mechanical effects of along-strike variations in nearshore upper-crustal rigidity. Shaded volumes represent low-rigidity (green) and high-rigidity (red) nearshore upper crust, and the accretionary prism (yellow). In low-rigidity domains, a steep, deformable forearc backstop permits enhanced upper-plate shortening, producing higher nearshore relief and reduced slab loading. In high-rigidity domains, a gentle, rigid backstop suppresses upper-plate deformation, resulting in lower nearshore relief and increased loading of the subducting slab. Dashed lines denote the surface expression of upper-crustal structures, and the curved basal surface illustrates the subducting slab.

The modeled along-strike heterogeneity in upper-crustal terranes spatially correlates with multiple proxies of subduction mechanics, including coastal uplift and subsidence rates reflected by geodetic and geomorphic observations (*6*, *47*), and slab geometry with its bending (*32*, *51*). Also, along-strike segmentation in ETS recurrence intervals and tremor density relates to forearc terrane distribution, suggesting upper crustal rheology impacts stress accumulation and release along deeper plate interface (*4*, *31*). In south-central CSZ,

this segmentation is also expressed in topography: peak elevations are ~0.6–0.8 km higher in the low-Vp onshore Franciscan domain than in the high-Vp Siletz domain (**Fig. 1a** and **S9**), indicating greater long-term vertical growth where the upper plate is more deformable.

Despite this evidence, geodetic inversions typically assume a laterally homogeneous upper plate with uniform elastic properties (e.g., shear and Young's moduli of ~40 and ~100 GPa, respectively, with a constant Poisson's ratio of ~0.25), ignoring crustal architectural and compositional variance (*7–10*). Our tomographic results, however, reveal a ~30 GPa difference in Young's modulus and ~0.06 in Poisson's ratio between the rigid Siletz and the compliant onshore Franciscan terranes (**Fig. S12**). Differences of this magnitude are mechanically significant for megathrust locking and will alter the partitioning of interseismic deformation and bias geodetically inferred coupling patterns even under identical fault slip conditions (*12*). The systematic mechanical segmentation our modeling suggests informs the nearshore subduction dynamics in two distinct pathways: the differential lithostatic loading driving the along-strike variability of nearshore slab depth (*42*, *43*, *52*), and the rigidity difference controlling the partition of stress and strain from plate convergence between elastic strain accumulation and permanent (plastic) vertical deformation along the coast (*6*, *21*, *46*, *47*).

Our numerical modeling confirms that density contrasts alone reproduce the observed ~2 km along-strike variation in nearshore slab depth through differential lithostatic loading, without requiring changes in slab buoyancy or plate kinematics (**Fig. 9**). Capturing the full amplitude of coastal uplift, however, requires incorporating viscoelastic strain partitioning. While pure elastic models predict ~20–25% of the observed uplift contrast, viscoelastic simulations successfully reproduce the full ~2 mm/yr difference (**Fig. 9**). In these simulations, horizontal shortening is distributed between recoverable elastic strain and time-dependent viscous deformation. Uplift rates are not prescribed but emerge from the time-dependent redistribution of tectonic force between mechanically coupled forearc blocks under constant convergence (**Fig. S11**). Rather than just resisting horizontal stress, the lower-rigidity backstops facilitate permanent internal shortening.

To reduce the dependency of uplift-rate simulation on specific numerical formulation, we additionally derived a closed-form elastic estimate using linear constitutive relations under plane-strain conditions (Supplementary **Text S3**). Despite neglecting viscous deformation and time-dependent relaxation, the elastic solution predicts a substantial uplift-rate contrast (~0.5 mm/year), corresponding to ~25% of the observed along-strike difference. This indicates that upper-crustal elastic rigidity by itself can explain a partial but substantial portion of the uplift segmentation. However, when viscoelastic strain partitioning is incorporated, the model reproduces the full ~2 mm/yr uplift contrast between high- and low-rigidity segments. Achieving this requires a large contrast in Maxwell relaxation time between terranes that is ~250 years for the low-rigidity Franciscan domain and ~50,000 years for the high-rigidity Siletz domain (a difference exceeding two orders of magnitude). Because Maxwell time scales with the ratio of effective viscosity to shear modulus, this contrast implies fundamentally different capacities for time-dependent strain accommodation within the forearc.

Such rheological contrasts are physically plausible for subduction settings (*53*). In exhumed subduction interface and mélange shear zones, which are appropriate analogs for weak sediment-dominated forearc materials, the compiled and field based estimates indicate effective viscosities in the range of 10^{18}-10^{20} Pa·s (*54*). For typical crustal shear moduli (20 – 40 GPa), these values naturally correspond to Maxwell times spanning a few hundred years (~100 – 300 years), consistent with our value of 250 years for low-rigidity

crust and supporting the interpretation that permanent (time-dependent) deformation can be efficient in the onshore Franciscan terrane. In contrast, compositionally strong crustal domains, such as the dry mafic crust, can sustain substantially higher effective viscosities, often exceeding ~10^{21} Pa·s (*55*, *56*). For shear moduli of 40 – 70 GPa, appropriate for coherent mafic crust, viscosities of 10^{22}-10^{23} Pa·s correspond to Maxwell relaxation time of 10^{4}-10^{5} years. These values are consistent with our high-rigidity end member (~50,000 yr), implying that a Siletz-like mafic backstop can behave effectively elastically over many earthquake cycles, while adjacent weak forearc domains relax on interseismic to century timescales.

Implications for geodetic locking models

Our results show that reliability of geodetically inferred megathrust locking depends systematically on overriding plate mechanics. In high-rigidity domains like the intact Siletz terrane, the forearc acts as a long-lived elastic buttress with negligible internal shortening. As a result, onshore surface velocities closely reflect elastic loading from the megathrust, providing a comparatively direct and robust constraint on the locking state. Conversely, beneath low-rigidity forearc domains, surface deformation is a complex superposition of elastic strain accumulation and permanent internal shortening.

Similar geodetic signals can be produced by markedly different combinations of megathrust locking and upper-plate rheology. More complications can arise when a significant part of interseismic vertical motion is retained over multiple earthquake cycles, rather than being fully recovered by coseismic and postseismic slip (*47*). Also, long-term coastal signal can depend on inelastic strain localization (e.g., occur within weak material adjacent to a rigid backstop, or via wedge faulting and plastic shortening), producing permanent uplift that pure elastic kinematic models fail to predict (*6*, *21*). In addition to elasto-plastic loading of the sedimentary wedge (*21*, *46*), other processes, such as sediment underplating, seamount subduction, tectonic erosion, and changing frictional coupling can also drive or modulate coastal uplift (*57*). Another limitation can be that slab dip variation leading to a change in downdip width (and thus surface area) of the locked interface can alter the integrated plate coupling force and the magnitude of horizontal compressive tractions transmitted into the upper plate (*58*). Furthermore, we did not explicitly vary the accretionary wedge geometry between segments. Yet wedge taper, basal dip, and the partitioning between outer- and inner-wedge deformation can vary substantially along strike (*46*). Nonetheless, even under these simplified conditions, our models demonstrate that upper-crustal rigidity contrasts alone provide a physically consistent explanation for the observed along-strike differences in slab depth and coastal uplift. Even when upper mantle relaxation is considered (*8*), the magnitude of relaxation-driven uplift is not independent of upper-plate structure, as its density contrasts modulate the buoyancy and stress transmitted to the mantle. Therefore, denser, more mafic terranes suppress relaxation-driven uplift relative to lower-density sedimentary forearc regions (Supplementary **Text S4**).

Reconciling near-trench deformation, coastal uplift, and along-strike locking segmentation requires integrating seafloor geodesy (*59*, *60*). We show that onshore geodetic measurements on rigid forearc terranes remain spatially distant and minimally affected from updip portion of the megathrust, where locking gradients, slow slip, and stress heterogeneity are expected to be strongest. Also, since the mechanically weak forearc can absorb a substantial fraction of interseismic shortening, onshore geodesy alone cannot distinguish between reduced locking and enhanced upper plate compliance (**Fig. 10**). Integrating offshore geodesy with spatially variable upper-plate structure offers a path toward physically consistent locking models. Where high-resolution tomography is

unavailable, mapped lithologic assemblages and terrane boundaries offer a practical proxy for prescribing laterally variable elastic properties in geodetic models. This approach reduces bias by accounting for spatial differences in upper-plate mechanical response, rather than misattributing all surface deformation variability entirely to changes in megathrust friction.

Implications for megathrust rupture

Beyond shaping slab flexure and interseismic uplift, upper-plate rigidity contrasts can significantly influence coseismic rupture segmentation, slip magnitude, and tsunami potential. Variations in forearc composition and elastic strength impose persistent along-strike controls on megathrust coupling (*61*, *62*). Denser, mechanically robust overriding plates accumulate elastic strain more efficiently, promoting stronger locking and larger, coherent coseismic slip patches—contrary to predictions from some uniform locking models (*7*). Conversely, weaker or heterogeneous domains can promote interseismic creep and distributed deformation, limiting stress accumulation. Applied to Cascadia, this implies that weaker forearc segments will likely favor partial rupture, yield reduced slip amplitudes, or act as persistent barriers to rupture propagation during a future great earthquake (*32*, *63*).

Furthermore, lateral and depth-dependent variations in upper-plate rigidity directly modulate shallow rupture behavior and tsunami generation, even in the absence of changes in fault friction (*64*). Compliant upper plates favor larger shallow slip, slower rupture velocities, and enhanced slip-rate amplification (*12*). This translates directly into greater seafloor deformation and heightened tsunami potential. Consequently, models assuming an overly rigid, uniform forearc systematically underestimate shallow deformation and tsunami amplitudes. Ultimately, accurately representing spatially variable upper-plate elastic structure is essential for realistic earthquake rupture modeling and tsunami hazard assessment, as treating the overriding plate as mechanically uniform obscures critical controls on shallow megathrust behavior.

MATERIALS AND METHODS

Seismic tomographic inversion

We develop a 3-D high resolution shore crossing P-wave velocity (Vp) model by jointly inverting active source travel times recorded offshore and onshore. The data combine CASIE21 marine air-gun shots (*32*) recorded by ocean bottom seismometers (OBS) (*65*) with wide-angle refractions recorded by Cascadia2021 onshore nodal array (*5*). For this study we use 11 CASIE21 shot lines recorded on 345 stations (6 permanent PNSN broadband stations, 28 OBS, and 311 temporary nodal stations), yielding 28,191 shot gathers (**Fig. 1a**). We manually pick 617,637 arrivals in total, including 598,082 first-arriving P phases and 19,557 PmP reflections from the oceanic Moho, providing dense multi-azimuth ray coverage from the accretionary prism to ~100 km onshore (**Fig. S2**). Travel times are picked on reduced-time record sections using the Matlab-based tlPicker package and assigned phase-dependent uncertainties (*5*). We pick Pg/Pn first arrivals where separable on shore-crossing profiles and PmP reflections where coherent; along-strike gathers where Pg and Pn are difficult to distinguish are treated as generic P first arrivals. Average picking uncertainties are 41 ms (Pg), 35 ms (Pn), 62 ms (P), and 63 ms (PmP). Data quality varies systematically with environment: near-shore stations are noisier due to ocean-wave microseisms, whereas inland nodal stations typically allow picks on ~40–60% of shots; offshore OBS record sections generally yield fewer reliable picks (<40% of shots) (*5*).

To improve phase identification and stabilize the nonlinear inversion, we use forward modeling to generate synthetic travel times from a suite of plausible starting models. The preferred initial Vp model is laterally and vertically smooth, with Vp increasing from ~2–5.5 km/s in the accretionary prism to >5.5 km/s in the Siletz terrane. We embed a 6-km-thick oceanic crust with Vp ~6.1–6.8 km/s and prescribe an upper-mantle Vp of 8.1 km/s beneath the slab (**Fig. S12**). We apply a convolution with a moving average from the top depth to the bottom of the model to make the model vertically smooth. We use a smooth slab geometry combining high-resolution offshore CASIE21 basement data and low-resolution onshore Moho model (*66*). We also perform a "Pg-fit" preliminary inversion (Pg only, without slab/mantle) to refine upper-crustal velocities, then re-insert slab and mantle structure before the final joint inversion of all phases.

Tomographic inversion follows the travel-time tomography formulation of (*67*), which is well suited to strongly heterogeneous amphibious data sets (*5*, *68*). We parameterize the model in slowness on a 3-D grid with 800-m node spacing in x, y, and z. Bathymetry and topography are incorporated by vertically shearing grid columns to honor local relief. Predicted travel times are computed using a shortest-path (graph-theory) solution to the two-point ray-tracing problem, which efficiently approximates first-arrival ray paths in complex 3-D velocity fields. Travel times through the water column are computed on a finer 50 × 50-m horizontal grid using a constant water velocity of 1.49 km/s to reduce sensitivity to bathymetric roughness. The inverse problem is linearized to relate travel-time residuals (observed minus predicted) to perturbations in model slowness, and, when PmP is included, to perturbations of the oceanic Moho interface (*69*). We solve for slowness (and interface) updates using damped least squares, minimizing a functional that balances (i) data misfit weighted by pick uncertainties, (ii) a penalty term that limits deviation from the prior model, and (iii) separate horizontal and vertical smoothing constraints. The inversion is iterated to account for ray-path changes, using a creeping strategy so that regularization acts on the cumulative perturbation after each iteration. After each inversion, we examine phase-specific residuals, repick or remove inconsistent arrivals, and continue iterating until the RMS residual converges (~50 ms), comparable to the typical picking uncertainty.

Model coverage and resolution are evaluated using the derivative weight sum (DWS), which provides a quantitative measure of the cumulative sensitivity of the travel-time data to velocity perturbations at each model node (**Fig. S2**). DWS is defined as the sum of the absolute partial derivatives of all travel times with respect to slowness at a given node and therefore reflects both ray density and raypath geometry. High DWS values indicate regions that are strongly constrained by the data through multiple ray paths sampling the node from different directions, whereas low DWS values indicate weakly constrained regions regardless of inversion regularization. Based on the distribution of DWS values and consistency with previous active-source tomographic studies, we restrict geological interpretation to regions with DWS $\geq$ 10, which correspond to areas of robust ray coverage.

The model's resolution was evaluated using a checkerboard test that involved inverting synthetic travel times through a perturbed Vp model containing 3-D sinusoidal patterns (see **Supplementary Text S1** and **Fig. S4** for details). Results demonstrate reliable pattern recovery in the nearshore region for 15 km spatial checkers, indicating that interpreted structures near the shoreline are not significantly biased by ray path geometry. While some east-west and vertical smearing occurs farther inshore or near model edges due to reduced crossing ray coverage, the north-south resolution remains robust throughout the study area. Ultimately, the nearly perfect recovery of larger checkers at depth confirms

that the tomographic model can reliably resolve the significant along-strike structural changes observed across the margin.

Conversion of velocity constraint to mechanical properties

After we establish the detailed velocity structure of the nearshore subduction zone, we perform numerical simulations to understand the mechanical behavior of CSZ. To do that, we convert the modeled velocities to elastic properties. First, we assign a range of Vp and Vs (S-wave velocity) values for each different tectonic block (i.e., accretionary prism, subducting slab, offshore terrane, onshore or nearshore terrane). To assign Vs values for the onshore terrane, we use the community velocity model of the Cascadia Region Earthquake Science Center (**Fig. S13**). For other tectonic blocks (i.e., accretionary prism and offshore terranes), we assume a Vp/Vs of 2.

Then we convert the Vp to density (ρ, in g/cm^3) using empirical equations gathered from (*70*). For Vp values greater than 6 km/s, indicative of materials like basalt, diabase, and gabbro, we use the equation from (*71*),

$$\rho = 2.4372 + \ 0.0761\, V_p \quad (1)$$

Conversely, for Vp values less than 6 km/s, typically associated with sedimentary rocks, the density is calculated using an equation derived by (*72*)

$$\rho = 1.74\, V_p^{0.25} \quad (2)$$

We then derive the mechanical properties from these seismic velocities (Vp, Vs). The shear modulus μ and Young's modulus E are calculated as

$$\mu = \rho\, V_s^2 \quad (3)$$

$$E = 2\mu(1+\nu) \quad (4)$$

Poisson's ratio ν is derived from the velocity ratio,

$$\nu = \frac{\left(\frac{V_p}{V_s}\right)^2 - 2}{2\left[\left(\frac{V_p}{V_s}\right)^2 - 1\right]} \quad (5)$$

The Young's modulus and Poisson's ratio determine the scalar flexural rigidity D_x at every node,

$$D_x = \frac{ET_e^3}{12(1-\nu^2)} \quad (6)$$

Numerical modeling setup

After converting the Vp from our tomographic inversion to density and elastic parameters, we develop a numerical framework to simulate both the flexural bending of the subducting slab and interseismic coastal uplift. Our model simplifies complex tectonic features into a generalized representation of the margin's first-order elements, as illustrated in **Fig. 8a**. The goal is to move beyond assumptions of lateral uniformity to evaluate how the variability in upper-plate rigidity directly modulates the geometry and stress state of the subduction zone.

Rather than assuming homogeneous plate properties, we explicitly incorporate upper-plate heterogeneity by subdividing the margin into four mechanically distinct tectonic elements arranged landward from the trench: the subducting oceanic plate, the accretionary prism, an offshore forearc unit (Terrane 1, representing the offshore Franciscan), and an onshore forearc unit (Terrane 2, representing the Siletz and onshore Franciscan). To capture the

evolving flexural response, the subducting slab is further partitioned into four along-profile zones corresponding to the incoming plate and the segments underlying the prism, Terrane 1, and Terrane 2, respectively. Within this framework, Terrane 2 is evaluated under two rheological end-members, a low-velocity or weak case and a high-velocity or strong case, representing the minimum complexity required to capture observed along-strike variations in seismic velocity and geodetic uplift.

To rigorously account for uncertainties in seismic velocities and rheological parameters, we execute the flexure and uplift simulations within a Monte Carlo framework. We perform 10,000 realizations, where Vp and Vs values are randomly and uniformly sampled from prescribed ranges for each tectonic component. This stochastic approach ensures that our model results are robust against local velocity fluctuations and allows us to quantify the sensitivity of slab curvature and surface deformation to the specific elastic properties of the overriding terranes. We report ensemble means and probability distributions of slab deflection and coastal uplift rate, and we visualize uncertainty using cloud plots based on a random subset (2,000 realizations).

Numerical simulation of flexural slab bending

To investigate how along-strike variations in upper-plate density influence slab flexure, we model the subducting plate as an elastic beam subjected to spatially variable vertical loading and flexural rigidity. The model is formulated in two dimensions along a trench-perpendicular profile and solved using a finite-difference approximation to the Euler–Bernoulli beam equation, following classical thin-plate flexural theory. Although three-dimensional flexural models are required where elastic thickness varies sharply along strike, previous work has shown that 2-D variable-rigidity formulations adequately capture slab bending where lateral variations are smooth or can be parameterized at the scale of tectonic domains (*43*). Given our focus on first-order mechanical contrasts associated with forearc terrane segmentation, a 2-D approach provides a computationally efficient framework for isolating the influence of upper-plate rigidity on slab bending.

Mechanical properties within each element are parameterized using seismic velocities (Vp and Vs), which are converted to density and elastic moduli and used to define spatially variable flexural rigidity. Vertical loading arises from the combined effects of slab pull and the excess mass of the overlying accretionary prism and forearc crust relative to a reference water column. By prescribing geometry and material properties at the scale of tectonic domains rather than individual faults, the model isolates the first-order mechanical influence of upper-crustal segmentation on slab bending.

In the Euler-Bernoulli beam theory, the slab $w(x)$ is controlled by the balance between the internal stiffness of the lithosphere and the external buoyancy and tectonic loads. The governing differential equation is below

$$\frac{d^2}{dx^2}\left(D(x)\frac{d^2w}{dx^2}\right) + (\rho_m - \rho_w)gw = q(x) \quad (7)$$

Here, $D(x)$ is the flexural rigidity, ρ_m is the mantle density (3300 kg/m^3), ρ_w is the water density (1030 kg/m^3), g is the gravitational acceleration, and $q(x)$ is the effective vertical load. We then solve this fourth-order system (Eq. 7) using a finite difference method. We approximate the curvature $\frac{d^2w}{dx^2}$ at the node i using the central difference stencil

$$\frac{d^2w}{dx^2} \approx \frac{w_{i-1} - 2w_i + w_{i+1}}{\Delta x^2} \quad (8)$$

We construct the stiffness matrix A by applying the second derivative operator twice, incorporating the spatially variable rigidity $D(x)$ as a diagonal matrix M_D such that $A \approx$

$D_2 M_D D_2 + K$, where K represents the hydrostatic restoring force. The system was solved via linear inversion $w = A \backslash q$

For the inversion, we define the vertical load $q(x)$ as the excess weight of the crustal column relative to a reference water column

$$q(x) = g \cdot (M_{column} - M_{water}) \quad (9)$$

For the rigid upper crustal blocks (e.g., Siletz), the load is simply $q_{block} = (\rho_{crust} - \rho_{water})gh$. However, for the accretionary prism, we account for sediment compaction, where porosity ϕ decreases exponentially with depth z according to Athy's Law, $\phi(z) = \phi_0 e^{-z/\lambda}$, where ϕ_0 is the surface porosity (assumed 0.30) and λ is the compaction decay scale (assumed 3 km). Now, to derive the sediment mass, we assume the bulk density $\rho_{bulk}(z)$ at any depth is a mixture of grain density ρ_{grain} and fluid density ρ_{fluid}

$$\rho_{bulk}(z) = \phi(z)\rho_{fluid} + (1 - \phi(z))\rho_{grain} \quad (10)$$

Now, substituting the porosity function

$$\rho_{bulk}(z) = \rho_{grain} - (\rho_{grain} - \rho_{fluid})\phi_0 e^{-\frac{z}{\lambda}} \quad (11)$$

To find the total mass M_{sed} of a sediment column of thickness h, we integrated the bulk density from the surface (z = 0) to the base (z = h)

$$M_{sed} = \int_0^h \rho_{bulk}(z)\, dz \quad (12)$$

Now, substituting ρ_{bulk} from Equation 5,

$$M_{sed} = \int_0^h \left[\rho_{grain} - (\rho_{grain} - \rho_{fluid})\phi_0 e^{-\frac{z}{\lambda}}\right] dz \quad (13)$$

Solving this integral analytically yields the mas equation used in our simulation,

$$M_{sed} = \rho_{grain} h - (\rho_{grain} - \rho_{fluid})\phi_0 \lambda (1 - e^{-\frac{h}{\lambda}}) \quad (14)$$

The final effective load for the prism is,

$$q_{prism} = [M_{sed} - (\rho_{fluid} h)]g \quad (15)$$

Numerical simulation of interseismic uplift rate

To quantify how upper-plate mechanical variability influences coastal uplift during the interseismic period, we model forearc deformation using a time-dependent elastic–viscous framework. Interseismic uplift along subduction margins reflects the combined effects of elastic strain accumulation driven by ongoing plate convergence and time-dependent stress relaxation within the upper plate and shallow mantle, rather than purely elastic loading alone. Both theoretical and observational studies show that forearc deformation during the earthquake cycle is governed by this competition between elastic locking on the megathrust and viscous or inelastic accommodation within the overriding plate, producing spatially variable uplift and subsidence patterns along the coast (*21*, *46*).

We therefore represent interseismic deformation as the response of a mechanically segmented forearc to imposed convergence, where elastic strain accumulates on short timescales while viscous deformation progressively relaxes stress over longer timescales. This formulation captures key aspects of subduction earthquake-cycle mechanics inferred from analogue experiments and geodynamic models, including stress transfer from the locked megathrust into the upper plate (*21*). Recent geodetic analyses further demonstrate

that regional and local patterns of uplift in Cascadia are sensitive to upper-plate rheology and internal deformation, supporting the use of simplified viscoelastic representations to interpret observed coastal uplift rates (*6*)

For calculating the interseismic uplift rate of the forearc terrane blocks, we modeled the system as a Maxwell viscoelastic body (an elastic spring and viscous dashpot in a series) under plane-strain compression. First, we discretize the subduction system into three mechanical components arranged in series: the driving subducting slab, the offshore terrane (Terrane 1), and the onshore/nearshore terrane (Terrane 2). We calculate the axial stiffness k_i for each component as $k_i = \frac{E_i A_i}{L_i}$, where E_i is the Young's modulus, A_i is the cross-sectional area perpendicular to compression, and L_i is the length of the block in the direction of convergence. The total effective elastic stiffness K_{eq} of the system is derived from the series combination of these components,

$$\frac{1}{k_{eq}} = \frac{1}{k_{slab}} + \frac{1}{k_{Terrane1}} + \frac{1}{k_{Terrane2}} \quad (16)$$

We assume the total convergence velocity of the slab (V_{conv}) is conserved and partitioned into elastic deformation velocity ($V_{elastic}$) and viscous flow velocity ($V_{viscous}$). From Hooke's Law, stress relates to strain via stiffness k_{eq} as $F = k_{eq}x$. Differentiating with respect to time gives the elastic velocity

$$V_{elastic} = \frac{dx}{dt} = \frac{1}{k_{eq}} \frac{dF}{dt} \quad (17)$$

For the viscous component, stress σ relates to strain rate $\dot{\epsilon}$ via viscosity η such that $\sigma = \eta\dot{\epsilon}$. Converting to force ($F = \sigma A$) and velocity ($V_{viscous} = \dot{\epsilon}L$),

$$V_{viscous} = \frac{F}{\eta} \frac{L}{A} \quad (18)$$

Where L is the block length, and A is the cross-sectional area. In this equation, we parameterize the viscosity of the dashpot using a prescribed Maxwell relaxation time $T_m = \frac{\eta}{\mu}$, where μ is the shear modulus.

Substituting the components from Equations 17 and 18 back into the velocity conservation equation,

$$V_{conv} = \left(\frac{1}{k_{eq}} \frac{dF}{dt}\right) + \left(\frac{FL}{\eta A}\right) \quad (19)$$

Rearranging to solve for the rate of force change $\frac{dF}{dt}$

$$\frac{dF}{dt} = k_{eq}\left(V_{conv} - \frac{FL}{\eta A}\right) \quad (20)$$

This ordinary differential equation (ODE) describes how tectonic force evolves over time, transitioning from mostly elastic accumulation to mostly viscous deformation governed by the prescribed Maxwell relaxation time. We solve this ODE numerically to find the force $F(t)$ and its derivative dF/dt at the time of interest, which is the interseismic window.

Finally, the surface uplift rate is the vertical expansion resulting from horizontal compression (Poisson effect). The total horizontal strain rate $\dot{\epsilon}_{total}$ is the sum of elastic and viscous strain rates

$$\dot{\epsilon}_{total} = \dot{\epsilon}_{elastic} + \dot{\epsilon}_{viscous} = \left(\frac{1}{EA} \frac{dF}{dt}\right) + \left(\frac{F}{\eta A}\right) \quad (21)$$

The vertical uplift rate is then

Uplift rate = $\dot{\epsilon}_{total}\ \nu\ H_{block}$ ——————————————————— (22)

Where η is the Poisson's ratio and H_{block} is the block thickness.

References

1. K. Satake, K. Shimazaki, Y. Tsuji, K. Ueda, Time and size of a giant earthquake in Cascadia inferred from Japanese tsunami records of January 1700. *Nature* **379**, 246–249 (1996).

2. J. J. Clague, Evidence for large earthquakes at the Cascadia Subduction Zone. *Rev. Geophys.* **35**, 439–460 (1997).

3. K. Wang, R. Wells, S. Mazzotti, R. D. Hyndman, T. Sagiya, A revised dislocation model of interseismic deformation of the Cascadia subduction zone: REVISED DISLOCATION MODEL OF INTERSEISMIC DEFORMATION. *J. Geophys. Res.* **108** (2003).

4. M. R. Brudzinski, R. M. Allen, Segmentation in episodic tremor and slip all along Cascadia. *Geol* **35**, 907 (2007).

5. A. Ashraf, E. E. E. Hooft, D. R. Toomey, A. M. Tréhu, S. Nolan, E. A. Wirth, K. M. Ward, A High-Resolution 3-D P-Wave Velocity Structure of the South-Central Cascadia Subduction Zone From Wide-Angle Shore-Crossing Seismic Refraction Data. *JGR Solid Earth* **130**, e2024JB029525 (2025).

6. K. A. McKenzie, K. P. Furlong, M. W. Herman, Regional and Local Patterns of Upper-Plate Deformation in Cascadia: The Importance of the Down-Dip Extent of Locking Relative to Upper-Plate Strength Contrasts. *Tectonics* **41** (2022).

7. G. M. Schmalzle, R. McCaffrey, K. C. Creager, Central Cascadia subduction zone creep. *Geochem. Geophys. Geosyst.* **15**, 1515–1532 (2014).

8. S. Li, K. Wang, Y. Wang, Y. Jiang, S. E. Dosso, Geodetically Inferred Locking State of the Cascadia Megathrust Based on a Viscoelastic Earth Model. *J. Geophys. Res. Solid Earth* **123**, 8056–8072 (2018).

9. E. O. Lindsey, R. Mallick, J. A. Hubbard, K. E. Bradley, R. V. Almeida, J. D. P. Moore, R. Bürgmann, E. M. Hill, Slip rate deficit and earthquake potential on shallow megathrusts. *Nat. Geosci.* **14**, 321–326 (2021).

10. E. M. Sherrill, K. M. Johnson, N. M. Jackson, Locating Boundaries Between Locked and Creeping Regions at Nankai and Cascadia Subduction Zones. *JGR Solid Earth* **129**, e2024JB029346 (2024).

11. F. F. Pollitz, 3D Viscoelastic Models of Slip-Deficit Rate Along the Cascadia Subduction Zone. *JGR Solid Earth* **130**, e2024JB029847 (2025).

12. M. Prada, P. Galvez, J. Ampuero, V. Sallarès, C. Sánchez-Linares, J. Macías, D. Peter, The Influence of Depth-Varying Elastic Properties of the Upper Plate on Megathrust Earthquake Rupture Dynamics and Tsunamigenesis. *JGR Solid Earth* **126**, e2021JB022328 (2021).

13. S. Zhao, R. D. Müller, Y. Takahashi, Y. Kaneda, 3-D finite-element modelling of deformation and stress associated with faulting: effect of inhomogeneous crustal structures. *Geophysical Journal International* **157**, 629–644 (2004).

14. A. Tassara, Control of forearc density structure on megathrust shear strength along the Chilean subduction zone. *Tectonophysics* **495**, 34–47 (2010).

15. M. Métois, A. Socquet, C. Vigny, Interseismic coupling, segmentation and mechanical behavior of the central Chile subduction zone. *J. Geophys. Res.* **117**, 2011JB008736 (2012).

16. P. Audet, S. Y. Schwartz, Hydrologic control of forearc strength and seismicity in the Costa Rican subduction zone. *Nature Geosci* **6**, 852–855 (2013).

17. Y. Liu, Source scaling relations and along-strike segmentation of slow slip events in a 3-D subduction fault model. *JGR Solid Earth* **119**, 6512–6533 (2014).

18. P. I. Ioannidi, L. Le Pourhiet, P. Agard, S. Angiboust, O. Oncken, Effective rheology of a two-phase subduction shear zone: Insights from numerical simple shear experiments and implications for subduction zone interfaces. *Earth and Planetary Science Letters* **566**, 116913 (2021).

19. L. Giambiagi, J. Mescua, F. Bechis, A. Tassara, G. Hoke, Thrust belts of the southern Central Andes: Along-strike variations in shortening, topography, crustal geometry, and denudation. *Geological Society of America Bulletin* **124**, 1339–1351 (2012).

20. J. Kley, C. R. Monaldi, J. A. Salfity, Along-strike segmentation of the Andean foreland: causes and consequences. *Tectonophysics* **301**, 75–94 (1999).

21. M. Rosenau, J. Lohrmann, O. Oncken, Shocks in a box: An analogue model of subduction earthquake cycles with application to seismotectonic forearc evolution. *J. Geophys. Res.* **114**, 2008JB005665 (2009).

22. J. M. Schütt, D. M. Whipp, Controls on Continental Strain Partitioning Above an Oblique Subduction Zone, Northern Andes. *Tectonics* **39**, e2019TC005886 (2020).

23. A. D. Chapman, D. Yule, W. Schmidt, T. LaMaskin, "Middle Jurassic to Early Cretaceous tectonic evolution of the western Klamath Mountains and outboard Franciscan assemblages, northern California–southern Oregon, USA" in *From Terranes to Terrains: Geologic Field Guides on the Construction and Destruction of the Pacific Northwest*, A. M. Booth, A. L. Grunder, Eds. (Geological Society of America, 2021; https://pubs.geoscienceworld.org/gsa/books/book/2333/chapter/131791202/Middle-Jurassic-to-Early-Cretaceous-tectonic), pp. 73–130.

24. A. M. Trehu, I. Asudeh, T. M. Brocher, J. H. Luetgert, W. D. Mooney, J. L. Nabelek, Y. Nakamura, Crustal Architecture of the Cascadia Forearc. *Science* **266**, 237–243 (1994).

25. A. Ashraf, I. Filina, Zones of Weakness Within the Juan de Fuca Plate Mapped From the Integration of Multiple Geophysical Data and Their Relation to Observed Seismicity. *Geochem Geophys Geosyst* **24**, e2023GC010943 (2023).

26. R. Wells, D. Bukry, R. Friedman, D. Pyle, R. Duncan, P. Haeussler, J. Wooden, Geologic history of Siletzia, a large igneous province in the Oregon and Washington Coast Range: Correlation to the geomagnetic polarity time scale and implications for a long-lived Yellowstone hotspot. *Geosphere* **10**, 692–719 (2014).

27. T. A. Dumitru, J. Wakabayashi, J. E. Wright, J. L. Wooden, Early Cretaceous transition from nonaccretionary behavior to strongly accretionary behavior within the Franciscan subduction complex: ACCRETION IN THE FRANCISCAN COMPLEX. *Tectonics* **29**, n/a-n/a (2010).

28. J. T. Watt, D. S. Brothers, Systematic characterization of morphotectonic variability along the Cascadia convergent margin: Implications for shallow megathrust behavior and tsunami hazards. *Geosphere* **17**, 95–117 (2021).

29. W. P. Irwin, "Terranes of the Klamath Mountains, California and Oregon" in *Tectonic Evolution of Northern California: Sausalito to Yosemite National Park, California, June 28–July 7, 1989*, M. C. Blake, D. S. Harwood, R. J. McLaughlin, A. S. Jayko, W. P. Irwin, F. C. W. Dodge, D. L. Jones, M. M. Miller, T. Bullen, Eds. (American Geophysical Union, Washington, D. C., 1989; http://doi.wiley.com/10.1029/FT108p0019), pp. 19–32.

30. R. J. Burgette, R. J. Weldon, D. A. Schmidt, Interseismic uplift rates for western Oregon and along-strike variation in locking on the Cascadia subduction zone. *J. Geophys. Res.* **114**, 2008JB005679 (2009).

31. A. G. Wech, Cataloging Tectonic Tremor Energy Radiation in the Cascadia Subduction Zone. *JGR Solid Earth* **126**, e2021JB022523 (2021).

32. S. M. Carbotte, B. Boston, S. Han, B. Shuck, J. Beeson, J. P. Canales, H. Tobin, N. Miller, M. Nedimovic, A. Tréhu, M. Lee, M. Lucas, H. Jian, D. Jiang, L. Moser, C. Anderson, D. Judd, J. Fernandez, C. Campbell, A. Goswami, R. Gahlawat, Subducting plate structure and megathrust morphology from deep seismic imaging linked to earthquake rupture segmentation at Cascadia. *Sci. Adv.* **10**, eadl3198 (2024).

33. R. E. Wells, R. J. Blakely, A. G. Wech, P. A. McCrory, A. Michael, Cascadia subduction tremor muted by crustal faults. *Geology* **45**, 515–518 (2017).

34. R. C. McPherson, J. R. Patton, M. Hellweg, S. W. Smith, L. Dengler, A. Lomax, D. S. Dreger, Large Repeating Gorda Intraplate Earthquakes Occurring Along an Inherited Weak Zone near the Mendocino Triple Junction. *Seismological Research Letters* **96**, 3179–3188 (2025).

35. M. D. Petersen, A. M. Shumway, P. M. Powers, E. H. Field, M. P. Moschetti, K. S. Jaiswal, K. R. Milner, S. Rezaeian, A. D. Frankel, A. L. Llenos, A. J. Michael, J. M. Altekruse, S. K. Ahdi, K. B. Withers, C. S. Mueller, Y. Zeng, R. E. Chase, L. M. Salditch, N. Luco, K. S. Rukstales, J. A. Herrick, D. L. Girot, B. T. Aagaard, A. M. Bender, M. L. Blanpied, R. W. Briggs, O. S. Boyd, B. S. Clayton, C. B. DuRoss, E. L. Evans, P. J. Haeussler, A. E. Hatem, K. L. Haynie, E. H. Hearn, K. M. Johnson, Z. A. Kortum, N. S. Kwong, A. J. Makdisi, H. B. Mason, D. E. McNamara, D. F. McPhillips, P. G. Okubo, M. T. Page, F. F. Pollitz, J. L. Rubinstein, B. E. Shaw, Z.-K. Shen, B. R. Shiro, J. A. Smith, W. J. Stephenson, E. M. Thompson, J. A. Thompson Jobe, E. A. Wirth, R. C. Witter, The 2023 US 50-State National Seismic Hazard Model: Overview and implications. *Earthquake Spectra* **40**, 5–88 (2024).

36. J. J. Franczyk, I. P. Madin, C. J. M. Duda, J. D. McClaughry, Oregon Geologic Data Compilation, Release 7, Oregon Department of Geology and Mineral Industries (2020); https://d3itl75cn7661p.cloudfront.net/dogami/dds/p-OGDC-7.htm.

37. R. P. Kucks, Bouguer gravity anomaly grid for the conterminous US, United States Geological Survey, Open-File Report 02-414 (1999); https://mrdata.usgs.gov/gravity/bouguer/.

38. R. Wells, D. Bukry, R. Friedman, D. Pyle, R. Duncan, P. Haeussler, J. Wooden, Geologic history of Siletzia, a large igneous province in the Oregon and Washington Coast Range: Correlation to the geomagnetic polarity time scale and implications for a long-lived Yellowstone hotspot. *Geosphere* **10**, 692–719 (2014).

39. B. A. Phillips, A. C. Kerr, E. K. Mullen, D. Weis, Oceanic mafic magmatism in the Siletz terrane, NW North America: Fragments of an Eocene oceanic plateau? *Lithos* **274–275**, 291–303 (2017).

40. T. M. Brocher, Compressional and Shear-Wave Velocity versus Depth Relations for Common Rock Types in Northern California. *Bulletin of the Seismological Society of America* **98**, 950–968 (2008).

41. W. D. Mooney, A. Ginzburg, Seismic measurements of the internal properties of fault zones. *PAGEOPH* **124**, 141–157 (1986).

42. A. F. Arnulf, D. Bassett, A. J. Harding, S. Kodaira, A. Nakanishi, G. Moore, Upper-plate controls on subduction zone geometry, hydration and earthquake behaviour. *Nat. Geosci.* **15**, 143–148 (2022).

43. J. Zhang, Z. Sun, M. Xu, H. Yang, Y. Zhang, F. Li, Lithospheric 3-D flexural modelling of subducted oceanic plate with variable effective elastic thickness along the Manila Trench. *Geophysical Journal International* **215**, 2071–2092 (2018).

44. D. J. Shillington, A. Bécel, M. R. Nedimović, H. Kuehn, S. C. Webb, G. A. Abers, K. M. Keranen, J. Li, M. Delescluse, G. A. Mattei-Salicrup, Link between plate fabric, hydration and subduction zone seismicity in Alaska. *Nature Geosci* **8**, 961–964 (2015).

45. M. Ivandic, I. Grevemeyer, A. Berhorst, E. R. Flueh, K. McIntosh, Impact of bending related faulting on the seismic properties of the incoming oceanic plate offshore of Nicaragua. *J. Geophys. Res.* **113**, 2007JB005291 (2008).

46. K. Wang, Y. Hu, Accretionary prisms in subduction earthquake cycles: The theory of dynamic Coulomb wedge. *J. Geophys. Res.* **111**, 2005JB004094 (2006).

47. R. Jolivet, M. Simons, Z. Duputel, J. -A. Olive, H. S. Bhat, Q. Bletery, Interseismic Loading of Subduction Megathrust Drives Long-Term Uplift in Northern Chile. *Geophysical Research Letters* **47**, e2019GL085377 (2020).

48. R. W. Porritt, R. M. Allen, D. C. Boyarko, M. R. Brudzinski, Investigation of Cascadia segmentation with ambient noise tomography. *Earth and Planetary Science Letters* **309**, 67–76 (2011).

49. T. M. Brocher, Empirical Relations between Elastic Wavespeeds and Density in the Earth's Crust. *Bulletin of the Seismological Society of America* **95**, 2081–2092 (2005).

50. H. Kopp, N. Kukowski, Backstop geometry and accretionary mechanics of the Sunda margin: ACCRETION MECHANICS OF THE SUNDA MARGIN. *Tectonics* **22**, n/a-n/a (2003).

51. W. Bloch, M. G. Bostock, P. Audet, A Cascadia Slab Model From Receiver Functions. *Geochem Geophys Geosyst* **24**, e2023GC011088 (2023).

52. D. Bassett, A. Arnulf, S. Kodaira, A. Nakanishi, A. Harding, G. Moore, Crustal Structure of the Nankai Subduction Zone Revealed by Two Decades of Onshore-Offshore and Ocean-Bottom Seismic Data: Implications for the Dimensions and Slip Behavior of the Seismogenic Zone. *JGR Solid Earth* **127** (2022).

53. K. Wang, "Elastic and Viscoelastic Models of Crustal Deformation in Subduction Earthquake Cycles" in *The Seismogenic Zone of Subduction Thrust Faults*, T. H. Dixon, C. Moore, Eds. (Columbia University Press, 2007; https://www.degruyter.com/document/doi/10.7312/dixo13866-017/html), pp. 540–575.

54. A. L. Abila, W. M. Behr, J. Ruh, Strength of viscous subduction interfaces: A global compilation. *Geology* **53**, 105–108 (2025).

55. H. Wang, C. A. Currie, Crustal deformation induced by mantle dynamics: insights from models of gravitational lithosphere removal. *Geophysical Journal International* **210**, 1070–1091 (2017).

56. J. Muto, B. Shibazaki, Y. Ito, T. Iinuma, M. Ohzono, T. Matsumoto, T. Okada, Two-dimensional viscosity structure of the northeastern Japan islands arc-trench system. *Geophysical Research Letters* **40**, 4604–4608 (2013).

57. N. Litchfield, S. Ellis, K. Berryman, A. Nicol, Insights into subduction-related uplift along the Hikurangi Margin, New Zealand, using numerical modeling. *J. Geophys. Res.* **112**, 2006JF000535 (2007).

58. M. Bodmer, D. R. Toomey, E. E. E. Hooft, B. Schmandt, Buoyant Asthenosphere Beneath Cascadia Influences Megathrust Segmentation. *Geophys. Res. Lett.* **45**, 6954–6962 (2018).

59. J. B. DeSanto, D. A. Schmidt, M. Zumberge, G. Sasagawa, C. D. Chadwell, Near full locking on the shallow megathrust of the central Cascadia subduction zone revealed by GNSS-Acoustic. *Earth and Planetary Science Letters* **665**, 119463 (2025).

60. Y. Yokota, T. Ishikawa, S. Watanabe, T. Tashiro, A. Asada, Seafloor geodetic constraints on interplate coupling of the Nankai Trough megathrust zone. *Nature* **534**, 374–377 (2016).

61. D. Bassett, D. T. Sandwell, Y. Fialko, A. B. Watts, Upper-plate controls on co-seismic slip in the 2011 magnitude 9.0 Tohoku-oki earthquake. *Nature* **531**, 92–96 (2016).

62. D. Melnick, B. Bookhagen, M. R. Strecker, H. P. Echtler, Segmentation of megathrust rupture zones from fore-arc deformation patterns over hundreds to millions of years, Arauco peninsula, Chile. *J. Geophys. Res.* **114**, 2008JB005788 (2009).

63. B. Shuck, B. Boston, S. M. Carbotte, S. Han, A. Bécel, N. C. Miller, J. P. Canales, J. Hutchinson, R. Merrill, J. Beeson, P. Gurun, G. Littel, M. R. Nedimović, G. Savard, H. Tobin, Slab tearing and segmented subduction termination driven by transform tectonics. *Sci. Adv.* **11**, eady8347 (2025).

64. V. Sallares, C. R. Ranero, M. Prada, A. Calahorrano B., "Earthquake rupture properties and tsunamigenesis in the shallowest megathrust" (other, display, 2020); https://doi.org/10.5194/egusphere-egu2020-5809.

65. J. P. Canales, N. C. Miller, W. Baldwin, S. M. Carbotte, S. Han, B. Boston, H. Jian, J. Collins, D. Lizarradlde, CASIE21-OBS: An Open-Access, OBS Controlled-Source Seismic Dataset for Investigating the Structure and

Properties of the Cascadia Accretionary Wedge and the Downgoing Explorer-Juan de Fuca-Gorda Plate System. *Seismological Research Letters* (2023).

66. A. Ashraf, E. E. E. Hooft, Shoreline crossing Moho geometry of the Cascadia slab: CascadiaMoho1.0. *Seismica* **2.4** (2026).

67. D. R. Toomey, S. C. Solomon, G. M. Purdy, Tomographic imaging of the shallow crustal structure of the East Pacific Rise at 9°30′N. *J. Geophys. Res.* **99**, 24135–24157 (1994).

68. M. Bodmer, D. R. Toomey, B. VanderBeek, E. E. Hooft, J. S. Byrnes, Body Wave Tomography of the Cascadia Subduction Zone and Juan de Fuca Plate System: Identifying Challenges and Solutions for Shore-Crossing Data. *Geochem. Geophys. Geosyst.* **21** (2020).

69. R. A. Dunn, V. Lekić, R. S. Detrick, D. R. Toomey, Three-dimensional seismic structure of the Mid-Atlantic Ridge (35°N): Evidence for focused melt supply and lower crustal dike injection. *J. Geophys. Res.* **110**, 2004JB003473 (2005).

70. T. M. Brocher, "Compressional and Shear Wave Velocity Versus Depthin the San Francisco Bay Area, California: Rules for USGS Bay Area Velocity Model 05.0.0" (Open-File Report 05–1317, U.S. Geological Survey, 2005).

71. N. J. Godfrey, B. C. Beaudoin, S. L. Klemperer, Ophiolitic basement to the Great Valley forearc basin, California, from seismic and gravity data: Implications for crustal growth at the North American continental margin. *Geological Society of America Bulletin* **109**, 1536–1562 (1997).

72. G. H. F. Gardner, L. W. Gardner, A. R. Gregory, FORMATION VELOCITY AND DENSITY—THE DIAGNOSTIC BASICS FOR STRATIGRAPHIC TRAPS. *GEOPHYSICS* **39**, 770–780 (1974).

Acknowledgments

Funding:

National Science Foundation grant EAR-1946426

Author contributions:

Conceptualization: AA, EH

Methodology: AA, EH, DT

Investigation: AA, EH

Visualization: AA, EH, DT

Supervision: EH, DT

Writing—original draft: AA, EH

Writing—review & editing: AA, EH, DT

Competing interests: Authors declare that they have no competing interests.

Data and materials availability: All the data used in this study are publicly available. The seismic data acquired through stations of the Cascadia2021 experiment are available in PH5 format under network code Z4 2021 in the online repository of the Seismological Facility for the Advancement of Geoscience (SAGE), which is operated by the Earthscope Consortium. The OBS data can be accessed through network code YR 2021. The seismic shot information for the CASIE21 experiment is available through the Marine Geoscience Data System (MGDS) repository.

Supplementary Text

Text S1: Checkerboard resolution test

We use the checkerboard test to understand the model resolution and whether we can reliably resolve structures, especially in the nearshore region. First, we perturb the initial Vp model using 3-D sinusoids with alternating increases and decreases in amplitude of 20% in Vp values. This generates a checkerboard pattern with our assigned spatial scale. We then predict the travel time for ray paths, that correspond to the source-receiver geometry of the observed data, through this perturbed or checkerboard model. Using these synthetic travel times, we perform a tomographic inversion and evaluate the recovery of the checker pattern as an indicator of the model resolution.

We show the result of this test in **Fig. S4** using checkers with a spatial resolution of 15 km, both in along and across-strike direction of the subduction zone. The recovery of the checkers is reliable particularly in the nearshore regions both offshore and onshore. Resolution is remarkably good in the north-south direction with some east-west and vertical smearing especially farther inshore where crossing ray coverage is not as good. This result shows that the interpreted structures close to the shoreline (e.g., static backstop geometry) are not significantly biased by the ray path geometry. Farther from the shoreline, there is increased smearing in the east-west/across-strike direction due to fewer crossing rays near the model edge. Notably, there is minimal smearing in the north-south/along-strike direction, even near the edges of the model, showing that the model will resolve structural changes along the margin well. The east-west smearing decreases with larger checkers (~20 km). In the nearshore region, the recovery of larger checkers is nearly perfect. Even at around 10 km depth, we can reliably resolve along-strike changes in structures with our tomographic model **(Fig. S4)**.

Text S2: Psuedo-Vp Structure from Surface Geology

In this study, we construct a pseudo-Vp map from Oregon Department of Geology and Mineral Industries' (DOGAMI) surface geology (Franczyk et al., 2020) by grouping units into lithologic families and assigning each family a single shallow Vp–depth relation (valid for depths <4 km). These relations are developed by Brocher (2005, 2008), who compiled well logs, refraction data, and laboratory measurements to establish depth-dependent velocity functions and empirical regressions for different rock families. For our purposes, we directly adopted these published equations and applied them to the mapped lithologic families to generate the pseudo-Vp map.

General Group 1: Marine sedimentary lithologies

Family A: They are mostly average marine basin clastics such as basin plain mudstone; slope mudstone; mudstone; siltstone; fine grained sediments; sandstone; deltaic sandstone; shelf sandstone, limestone; dolomite; marble; marine sedimentary rocks; sedimentary rocks. The following equation applied to these lithologies is based on Older Cenozoic sedimentary rocks / average basin" relation.
Equation: $Vp = 2.24 + 0.60\ z$

Family B: They are mostly high Vp marine rocks such as chert; tuffaceous sedimentary rocks; coarse-grained sediments; conglomerate; quartzite; basalt. The equation applied is based on rocks from Salinas and the East Bay Trough.
Equation: $Vp = 4.354 + 0.74 (z - 3)$

Family C: These are turbidite; mixed-grained sediments, mixed lithologies. The equation is based on rocks from the Great Valley Sequence.
Equation: $Vp = 4.1675 + 0.4725 (z - 3)$

General Group 2: Terrestrial sedimentary lithologies

Family A: They are mostly average continental basin clastics such as fine grained sediments, mudstone, sandstone, mixed-grained sediments (typical fluvial–lacustrine interbeds). The equation is based on typical onshore basins such as the Great Valley, West Delta, and Livermore.
Equation: $Vp = 4.04 + 0.60 (z - 3)$

Family B: These are coarse-grained sediments and conglomerate. The equation is based on rocks from Miocene transtensional basin.
Equation: $Vp = 4.354 + 0.74 (z - 3)$

Family C**:** They are mostly interbedded sand–mud successions.
Equation: $Vp = 4.1675 + 0.4725 (z – 3)$

General Group 2: Metamorphic lithologies

Family A: They mostly fall within felsic metamorphic bedrock such as gneiss, schist, hornfels, quartzite, mixed metamorphic rocks.
Equation: $Vp = 6.18 + 0.159 (z - 3)$

Family B: These are mafic metamorphic bedrock. We have subdivided this family into three subdivisions.
First one is Amphibolite/Metagrabbro, with equation: $Vp = 7.002 + 0.002 (z - 3)$
Second one is Greenstone, with the equation: $Vp = 5.770 + 0.0584 (z - 3)$
Final one is Metabasalts, with equation: $Vp = 5.361 + 0.475 (z - 3)$

Family C: This is ultramafic metamorphic bedrock, which is mostly serpentinite with a Vp of 5.29 km/s.

Family D: This family belongs to carbonate metamorphic rocks, which mostly include marble that has a Vp of 3.37.

General Group 3: Intrusive rocks

Family A: They are felsic intrusive felsic composition lithologies that include nepheline syenite, rhyolite, and ambiguous mixed lithologies that are dominantly felsic. Also, carbonate crystalline

such as marble falls into this family. The Vp-depth relationship for this family is derived based on rocks from onshore Bay area crystalline.
Equation: $Vp = 6.18 + 0.159 (z - 3)$

Family B: They are of intermediate composition, such as andesite, basaltic andesite, dacite, rhyodacite, trachydacite, and other intermediate composition lithologies.
Equation: $Vp = 4.338 + 0.438 (z - 3)$

Family C: They are Mafic rocks which include mafic composition lithologies, basalt, basanite, and breccia/brecciated rock.
For Gabbro(intrusive), the equation: $Vp = 7 + 0.002 (z - 2)$
For Basalt (unaltered, extrusive), the equation: $Vp = 5.361 + 0.475 (z - 3)$

Family D: They are of ultramafic composition lithologies, which are mostly serpentinite (Vp = 5.29).

General Group 4: Mélange rocks

Family A: This family belongs to marine/forearc clastics such as mudstone, sandstone, conglomerate, mixed grained sediments, mixed lithologies, marine sedimentary rocks, sedimentary rocks, and turbidite. Equation for this family is based on the Franciscan metagraywacke matrix.
Equation: $Vp = 4.1675 + 0.4725 (z - 3)$

Family B: They are high-Vp marine siliceous/carbonate such as chert.
Equation: $Vp = 4.354 + 0.74 (z - 3)$

Family C: The rocks of this group belong to the felsic metamorphic/crystalline group, such as gneiss, schist, and hornfels. The equation is based on the granite/felsic relation.
Equation: $Vp = 6.18 + 0.159 (z - 3)$

Family D: Rocks of this family are mafic metamorphic such as greenstone, blueschist, metabasalts, and other mafic composition lithologies.
For greenstone, the equation is $Vp = 5.770 + 0.0584 (z - 3)$
For metabasalts, the equation is $Vp = 5.361 + 0.475 (z – 3)$

Family E: These rocks are of Ultramafic composition which is mostly serpentine (Vp = 5.29).

Family F: They are intermediate volcanic rocks such as dacite.
Equation: $Vp = 4.338 + 0.438 (z - 3)$

Family G: They are mafic volcanic rocks such as basalt, basanite.
Equation: $Vp = 5.361 + 0.475 (z - 3)$

Family H: They are carbonates such as limestone and marble. For limestone and marble, we use the same equation as Family A and Family C, respectively.

General Group 5: Volcanic rocks

The subdivided families for this group are the same as the general group 4.

General Group 6: Volcanic pyroclastic rocks

Family A: They are mafic volcanic (basaltic lavas).
Equation: Vp = 5.361 + 0.475 (z−3)

Family B: These are intermediate volcanic rocks such andesite, basaltic andesite and dacite lavas.
Equation: Vp = 4.338 + 0.438 (z−3)

Family C: Rocks of this family belong to felsic volcanic such as the massive rhyolite flows
Equation: Vp = 6.18 + 0.159 (z−3)

Family D: They are pyroclastic rocks such as tuff, ignimbrite, breccia, and tuffaceous.
Equation: Vp = 4.26 + 0.17 (z−1.5)

Text S3: Closed-form elastic estimate of coastal uplift

Here we present an analytical, closed-form calculation of interseismic coastal uplift based purely on linear elasticity. The purpose of this exercise is not to replace the numerical elastic/viscoelastic model using force evolution in the main text, but to provide an independent and transparent benchmark. By deriving uplift rates directly from constitutive relations, the goal is to demonstrate that even in the elastic limit—without invoking viscous flow or time-dependent relaxation—contrasts in upper-crustal rigidity produce a significant fraction of the observed along-strike uplift-rate difference.

In this calculation, we consider a simplified forearc represented by two elastic blocks (Terrane 1 and Terrane 2) arranged in series along the convergence direction x. Each block has length L_i, thickness H_i, Young's modulus E_i, and Poisson's ratio ν_i. Horizontal shortening is imposed by a constant far-field convergence rate V imposed across the combined length $L = L_1 + L_2$.

For an isotropic, linear elastic material under plane strain, the constitutive relation between stress and strain can be written in the form of generalized 3-D Hooke's law,

$$\epsilon_{xx} = \left(\frac{1}{E}\right)[\sigma_{xx} - \nu(\sigma_{yy} + \sigma_{zz})]$$
$$\epsilon_{yy} = \left(\frac{1}{E}\right)[\sigma_{yy} - \nu(\sigma_{xx} + \sigma_{zz})]$$
$$\epsilon_{zz} = \left(\frac{1}{E}\right)[\sigma_{zz} - \nu(\sigma_{xx} + \sigma_{yy})]$$

Now, we apply boundary conditions. First, we assume plane strain deformation, so $\epsilon_{yy} = 0$. Then the top surface is traction-free, so $\sigma_{zz} = 0$. This means

$0 = \left(\frac{1}{E}\right)[\sigma_{yy} - \nu(\sigma_{xx} + 0)] \Rightarrow \sigma_{yy} = \nu\sigma_{xx}$
After substituting $\sigma_{yy} = \nu\sigma_{xx}$ and $\sigma_{zz} = 0$,
$\epsilon_{zz} = \left(\frac{1}{E}\right)[0 - \nu(\sigma_{xx} + \nu\sigma_{xx})] = -\frac{\sigma_{xx}}{E}\nu(1+\nu)$
To express vertical strain in terms of horizontal strain, we similarly simplify ϵ_{xx},
$\epsilon_{xx} = \frac{\sigma_{xx}}{E}[1 - \nu^2]$
Taking the ratio gives the key elastic coupling under these boundary conditions,
$\frac{\epsilon_{zz}}{\epsilon_{xx}} = -\frac{\nu}{1-\nu} \Rightarrow \epsilon_{zz} = -\frac{\nu}{1-\nu}\epsilon_{xx}$

Also, vertical strain is related to the change in thickness of a block, $\epsilon_{zz} = \frac{\Delta H}{H}$ and horizontal strain is $\epsilon_{xx} = \frac{\Delta L}{L}$.
Now, based on this horizontal strain rate $\dot{\epsilon}_{xx} = \frac{d}{dt}\left(\frac{\Delta L}{L}\right) = \frac{1}{L}\frac{d(\Delta L)}{dt}$
However, for a block shortened at rate V_{conv} (positive toward shortening), $\frac{d(\Delta L)}{dt} = -V_{conv}$
So, the horizontal strain rate becomes $\dot{\epsilon}_{xx} = -\frac{V_{conv}}{L}$
Then, the vertical strain rate becomes $\epsilon_{zz} = \frac{\nu}{1-\nu}\frac{V_{conv}}{L} = \frac{\Delta H}{H}$
Therefore, the change in uplift $\Delta H = V_{conv}\left(\frac{\nu}{1-\nu}\right)\left(\frac{H}{L}\right)$

Using the plane-strain constitutive relation derived above, the horizontal stress–strain relation can be written as:
$\sigma_{xx} = \left(\frac{E}{1-\nu^2}\right)\epsilon_{xx}$
With $\sigma_{xx} = \frac{F}{A}$ and $\varepsilon_{xx} = \frac{\Delta L}{L}$, we obtain:
$\frac{F}{A} = \left(\frac{E}{1-\nu^2}\right)\left(\frac{\Delta L}{L}\right) \Rightarrow F = \left[\frac{EA}{L(1-\nu^2)}\right]\Delta L$

Now, when two elastic blocks are arranged in series, total convergence rate V_{conv} partitions into shortening rates V_1 and V_2 such that, $V_{conv} = V_1 + V_2$. Because the terranes are in series, they carry the same horizontal force F (force continuity): F1 = F2.

This motivates defining an effective elastic stiffness (per unit along-strike width) for terranes
$K_i = \frac{E_i A_i}{[L_i(1-\nu_i^2)]}$
Taking time derivatives yields $\frac{dF}{dt} = K_i$. And with $F_1 = F_2$, their rates are equal, so $K_1 V_1 = K_2 V_2$.
Then, combining with $V_{conv} = V_1 + V_2$ gives,
$V_1 = V_{conv}\left(\frac{K_2}{K_1+K_2}\right)$, $V_2 = V_{conv}\left(\frac{K_1}{K_1+K_2}\right)$

Substituting the partitioned convergence rate V2 into the single-block uplift relation gives the Terrane-2 uplift rate
$\dot{u_2} = V_2\left(\frac{\nu_2}{1-\nu_2}\right)\left(\frac{H_2}{L_2}\right) = V_{conv}\left(\frac{K_1}{K_1+K_2}\right)\left(\frac{\nu_2}{1-\nu_2}\right)\left(\frac{H_2}{L_2}\right)$

Here, K_1 and K_2 are computed using $K_i = \frac{E_i A_i}{[L_i(1-\nu_i^2)]}$. Because $A_i = H_i \cdot W$ (thickness times unit along-strike width W), W cancels in the ratio $\frac{K_1}{K_1+K_2}$, so only H_i, L_i, E_i, and ν_i are required.

We evaluate this closed-form expression using representative geometry of terranes from **Fig. 8**. Terrane2 thickness is approximately $H_2 \approx 30$ km. Terrane1 thickness increases from ~10 to ~15 km across the forearc; we use a representative average $H_1 \approx 12.5$ km. The along-dip extent of Terrane1 in the model spans roughly 60 km (from backstop1 at ~60 km to backstop 2 at ~120 km). Terrane 2 occupies the outer forearc; because shortening and uplift are distributed across a finite coastal belt rather than a single vertical interface, we use an effective shortening width $L_2 \approx$ 40 km for Terrane2 (this choice yields a conservative elastic contrast; using L_2 = 20 km increases the predicted contrast modestly).

Elastic properties of the terranes used in our calculation:
Terrane 1: E_1 = 40 GPa, ν_1 = 0.27.
Terrane 2 (low-rigidity end member): E_2 = 42 GPa, ν_2 = 0.29.
Terrane 2 (high-rigidity end member): E_2 = 71 GPa, ν_2 = 0.35.

With these constraints, Terrane2 (nearshore-onshore terrane) uplift rate follows, for the low-rigidity case, 2.86 mm/year, and for the high-rigidity case, it is 5.81 mm/year. Thus, this closed-form elastic end member predicts an uplift-rate contrast for Terrane2 around 0.5 mm/year, which is around 25% of the observed ~2 mm/year contrast. This shows that upper-crustal rigidity contrasts alone generate a substantial, physically inevitable component of uplift segmentation, providing an independent benchmark for the numerical simulations while motivating the additional time-dependent viscoelastic processes required to match the full amplitude of the observations.

Text S4: Effect of upper crustal density contrast in mantle relaxation driven uplift

The goal of this calculation is not to model the full interseismic uplift signal, which in the main text is treated using coupled elastic–viscoelastic simulations, but rather to isolate and quantify the contribution of upper-crustal density contrasts alone to mantle-relaxation-driven vertical motion. To estimate representative upper-crustal densities for the end-member terranes considered in this study, we convert Vp to density using empirical relationships compiled in the Materials and Methods. In low-rigidity forearc (Franciscan terrane), for Vp = 5.0 km/s, we get the density ρ_{low} = 2.60 g/cm^3. And in high-rigidity forearc (Siletz terrane), for Vp = 6.25 km/s, the density ρ_{high} = 2.91 g/cm^3.

Now the first order vertical velocity associated with mantle relaxation driven by a density contrast may be expressed as

$$V \propto \frac{(\rho_m - \rho_c) g h L}{\eta_m}$$

Where ρ_m is mantle density, ρ_c is crustal density, g is gravitational acceleration, h is the amplitude of the vertical load or deflection transmitted to the mantle, L is the characteristic lateral length scale of relaxation, and η_m is the mantle viscosity. Holding all parameters constant, except ρ_c, isolates the effect of upper-crustal density alone. Now, assuming a mantle density of

ρ_m = 3.30 g/cm^3, the effective density contrast for low rigidity crust $\Delta\rho_{low}$ = 0.70 g/cm^3 and for high rigidity crust $\Delta\rho_{high}$ = 0.39 g/cm^3

The ratio of relaxation-driven uplift rates between the two terranes is therefore

$$\frac{V_{high}}{V_{low}} = \frac{\Delta\rho_{high}}{\Delta\rho_{low}} = 0.56$$

This result implies that, purely due to density contrasts, mantle-relaxation-driven uplift beneath the Siletz terrane would be approximately 40–45% lower than beneath the Franciscan terrane, if mantle viscosity and tectonic forcing are identical.

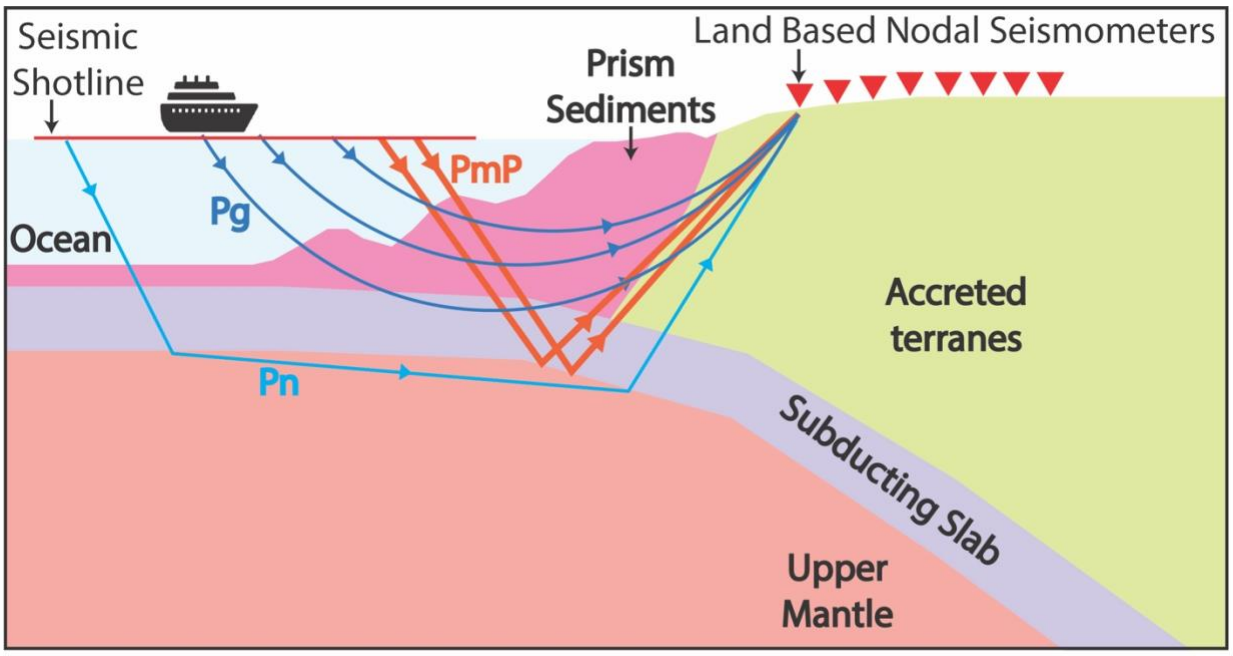

Fig. S1.
Schematic of the amphibious active-source seismic experiment used for the shore-crossing tomographic inversion. A marine seismic source (air-gun array) was fired along offshore shot lines and recorded by both offshore instruments and land-based nodal seismometers deployed across the coastline. Representative ray paths illustrate the phases used in the inversion: Pg refractions sampling the upper crust, Pn refractions traveling within the upper mantle, and PmP reflections from the oceanic Moho beneath the subducting slab. The experiment geometry enables continuous ray coverage from the offshore accretionary prism and prism sediments, across the shoreline, and into the onshore accreted terranes, providing joint constraints on shallow crustal velocity structure and slab geometry.

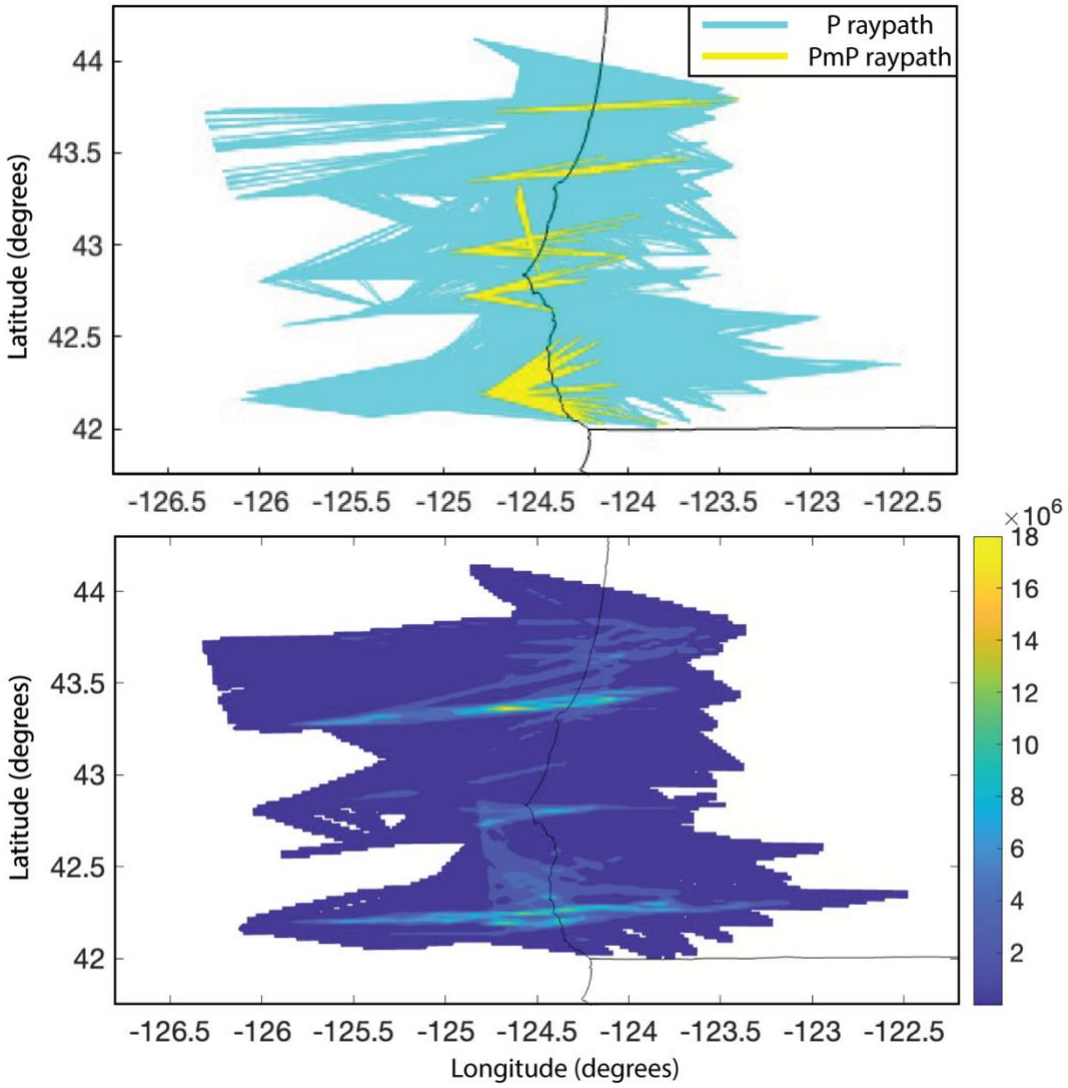

Fig. S2.

Raypath coverage and derivative weight sum (DWS) for the 3-D tomographic model. Top panel shows map views of representative seismic raypaths used in the tomographic inversion. Light-blue lines show Pg,Pn/P arrivals, with every 100th P arrival plotted for clarity, and yellow lines show PmP arrivals, with every 10th PmP arrival plotted. The distribution illustrates shore-crossing ray coverage from offshore sources to onshore receivers across the study area. The bottom panel shows DWS of the tomographic model, representing the cumulative sensitivity of travel-time observations to velocity perturbations within each model cell. Higher DWS values indicate stronger ray coverage and better-constrained regions of the model. We use DWS>10 to mask the contour plots of the tomographic model shown in this paper.

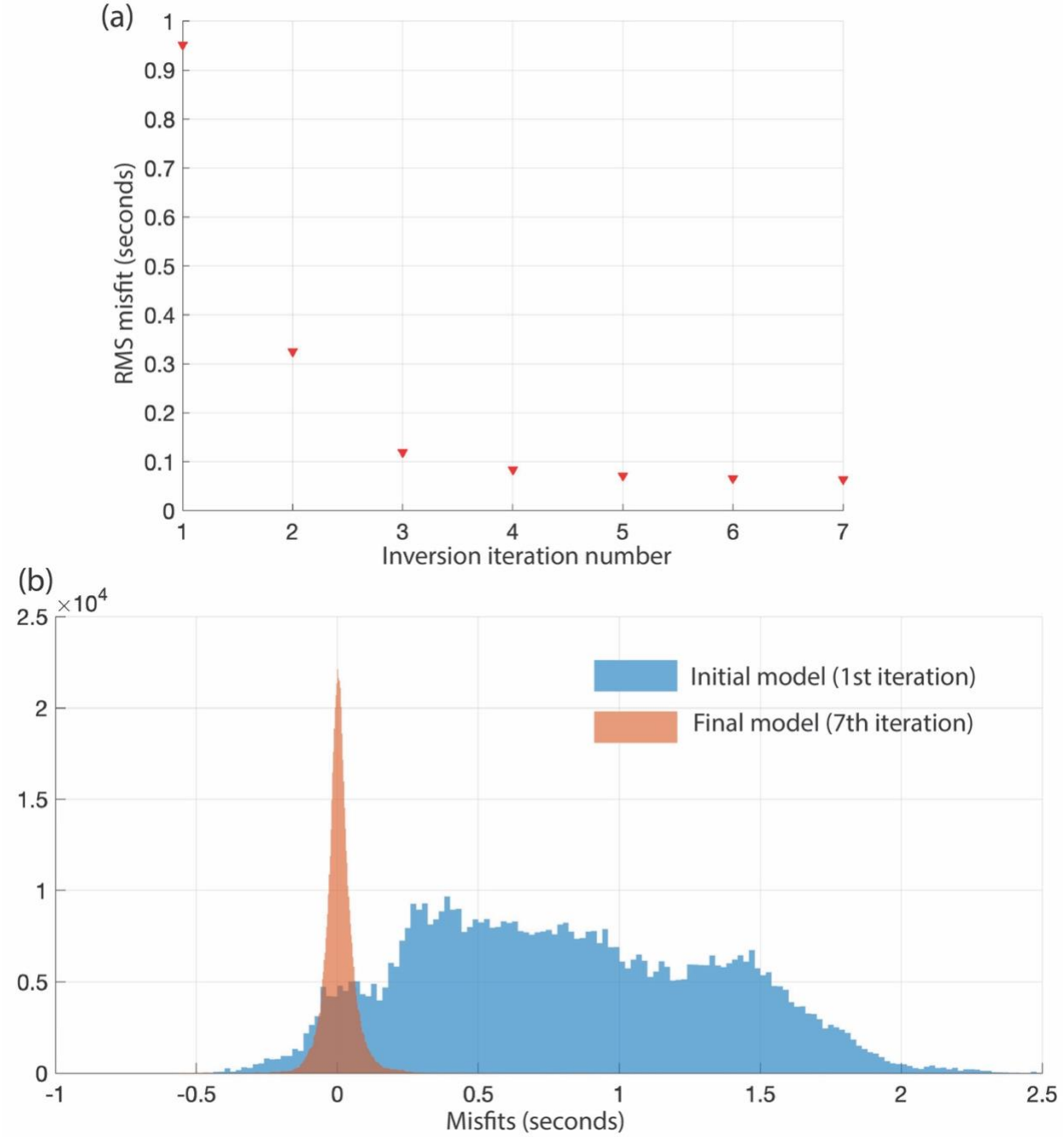

Fig. S3.

Graphs representing residual misfits (difference between observed and calculated seismic arrivals) of our tomographic inversion. (a) RMS misfit for each iteration of the inversion. (b) Histogram of misfits for the first and final iteration.

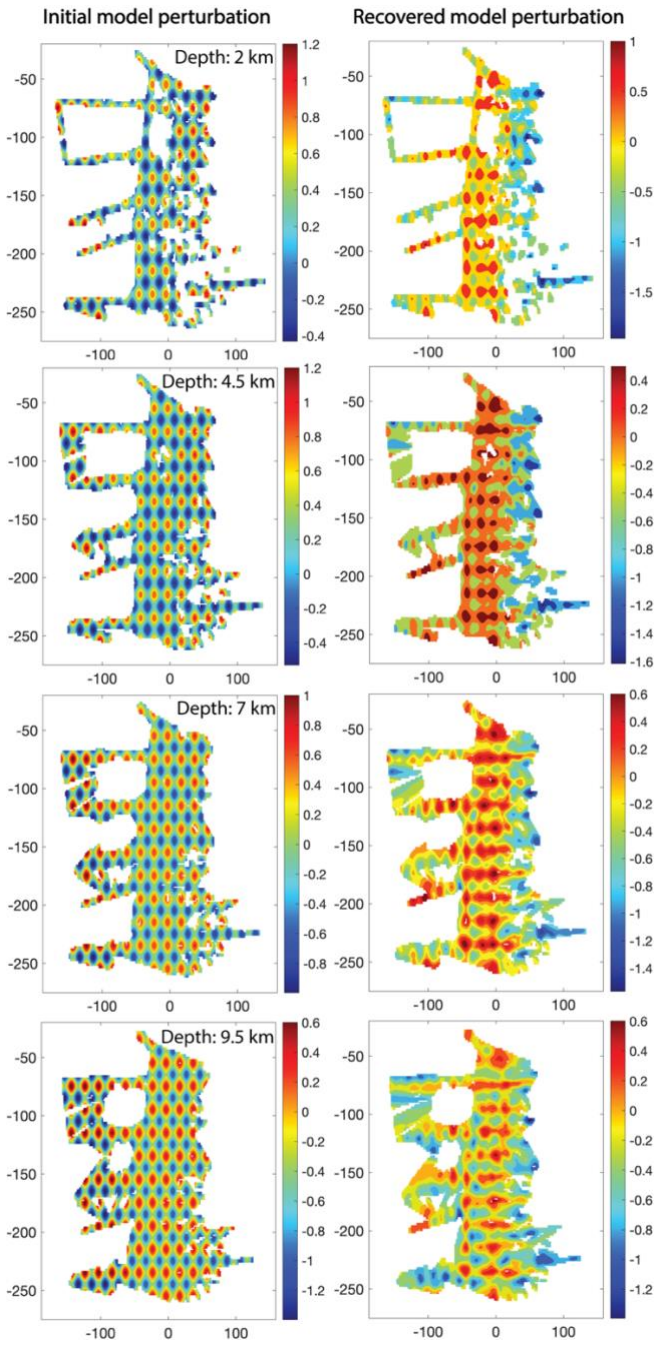

Fig. S4.
Checkerboard resolution test for the 3-D Vp tomographic inversion. Left panels show the imposed initial model perturbation, generated by applying 3-D sinusoidal checkerboard anomalies with ±20% Vp amplitude and a characteristic wavelength of ~15 km in both along-strike and across-strike directions. Right panels show the recovered model perturbation obtained by inverting synthetic travel times calculated through the checkerboard model using the same source–receiver geometry, phase selection, and inversion parameters as the observed data. Maps are displayed in kilometers in the horizontal (x–y) directions; the central ±25 km in the x-direction corresponds to the nearshore region.

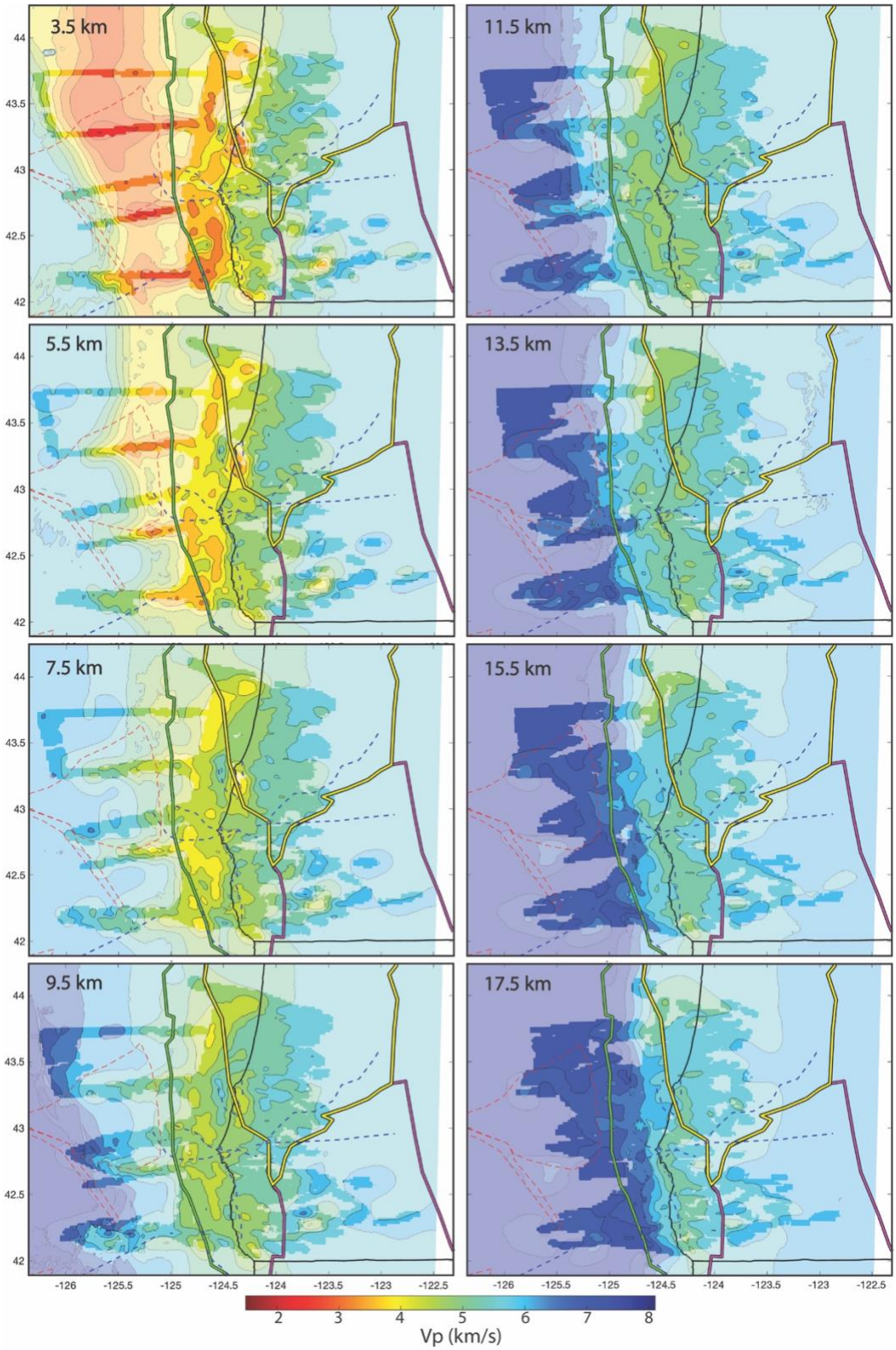

Fig. S5.
Map sections at every 2 km intervals of the Vp tomographic model. Symbology is similar to **Figs. 1** and **2**.

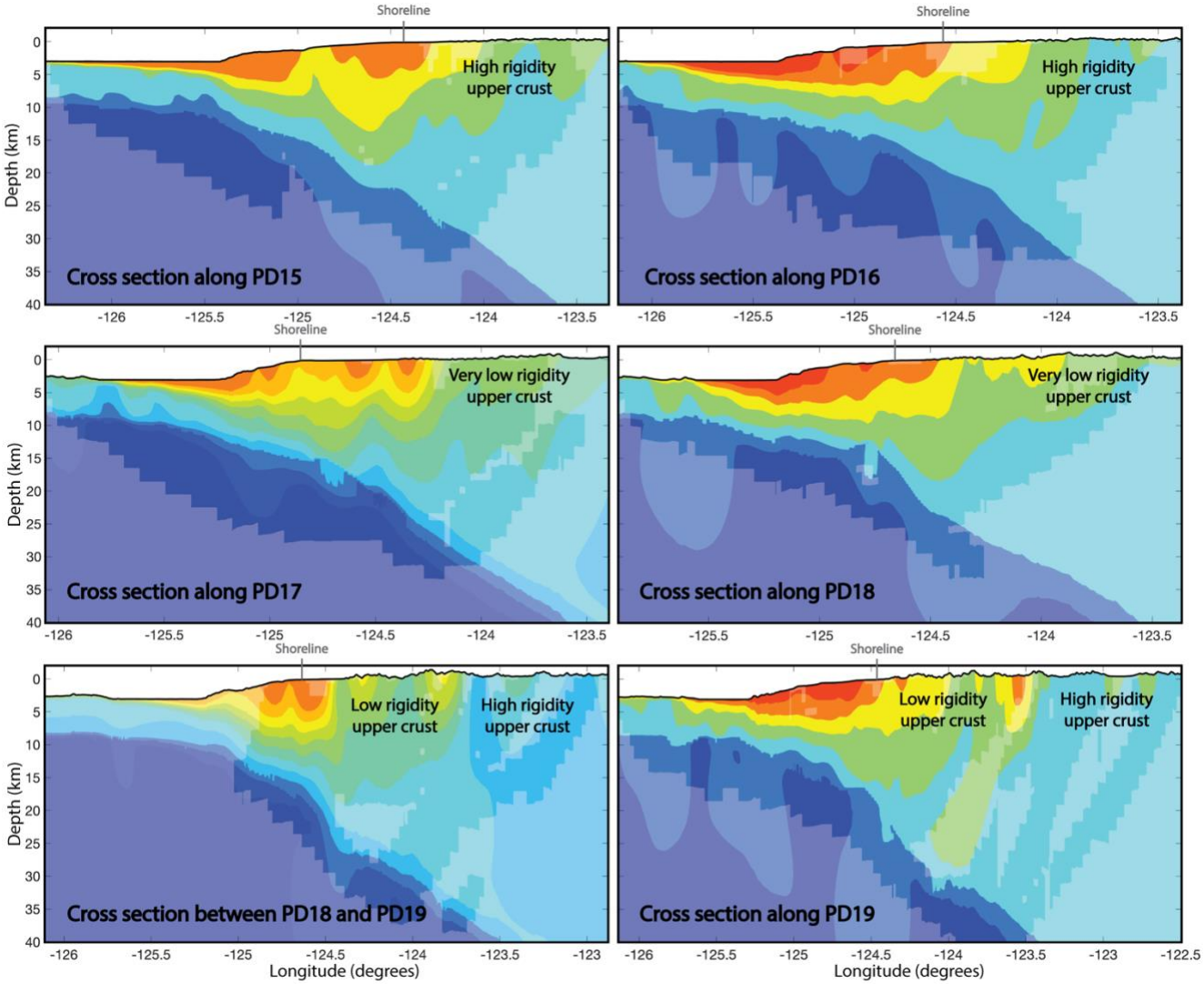

Fig. S6.
Cross-sections of the Vp tomographic model along all the east-west offshore seismic shotlines and onshore dense nodal stations. The symbology and colorbar follow **Figs. 2, 3, S4**.

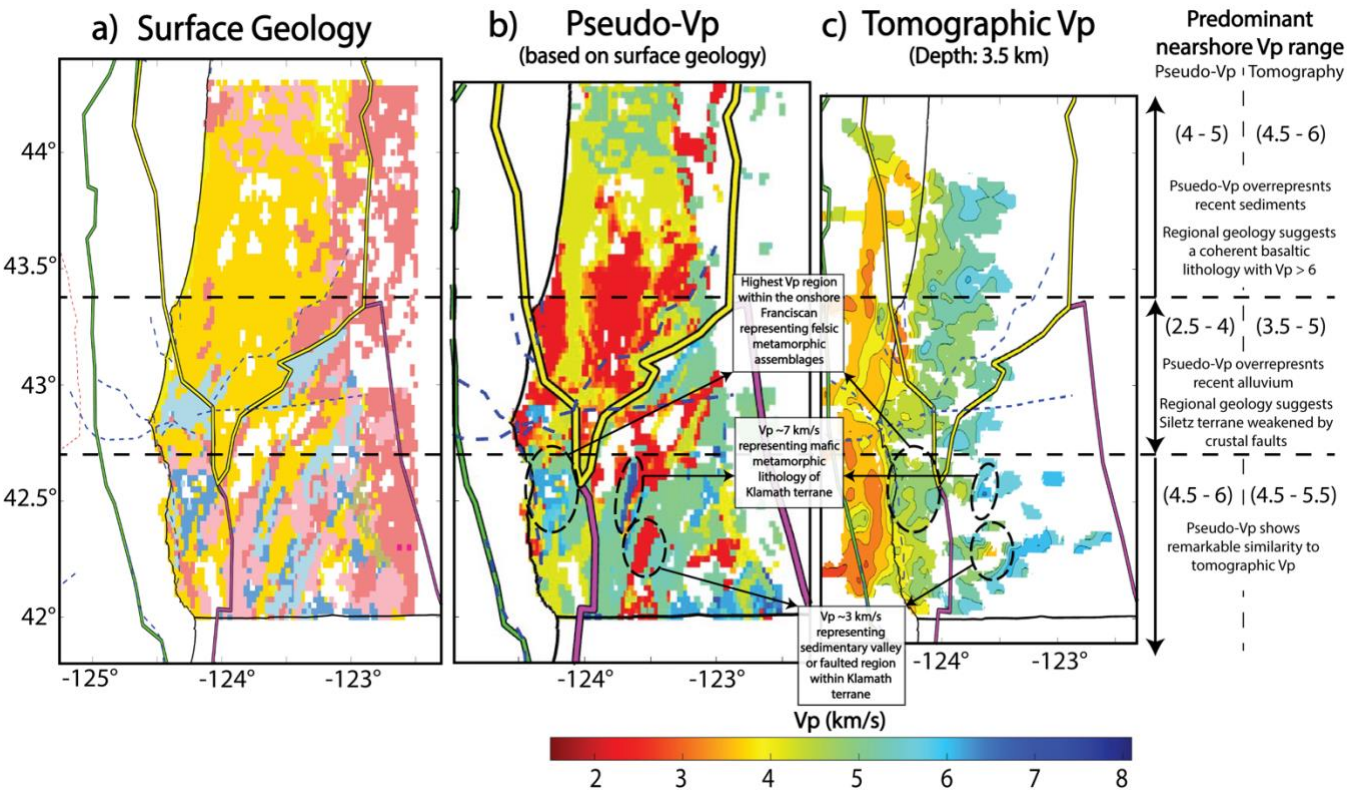

Fig. S7.

Comparison of surface geology and our seismic velocity model. (a) Surface geology of the study area (as in **Fig. 1b**) resampled to match the grid spacing of the tomographic model. (b) Pseudo-Vp map generated for a depth of 4 km based on empirical lithology-velocity relationships (see Supplementary **Text S2**) derived from surface geology. (c) Tomographic Vp model at 3.5 km depth (refer to **Fig. S5** for other map sections of the model). The panel to the right provides a latitudinal comparison of predominant nearshore Vp ranges (km/s) between the pseudo and tomographic Vp. Notes highlight if the surface-based estimates underrepresent subsurface geology and whether our knowledge of regional geology has to be invoked to better constrain expected Vp at depth. The dashed circles in 'b' and 'c' connected by black arrows represent regions with similar velocity between pseudo and tomographic-Vp which illustrate that surface geology based Vp calculation can closely approximate the Vp from tomographic modeling.

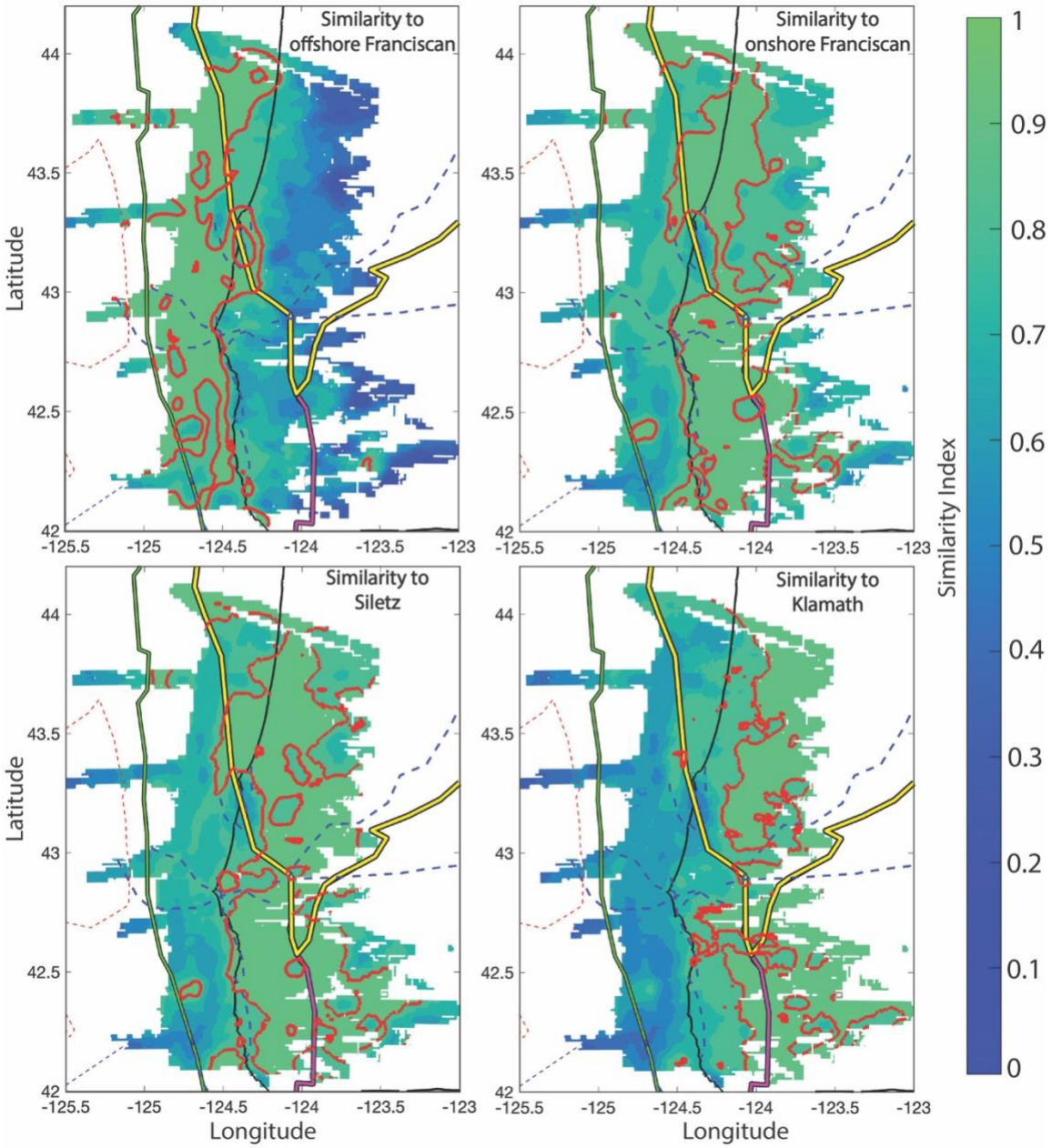

Fig. S8.
Similarity analysis between tomographic velocity structure and terrane-averaged reference profiles. Maps show the spatial distribution of the similarity index (0–1) between local 1-D Vp–depth profiles extracted from the 3-D tomographic model and terrane-averaged reference velocity profiles for the offshore Franciscan, onshore Franciscan, Siletz, and Klamath terranes. Warmer colors indicate higher similarity. Red contours outline regions exceeding a high similarity threshold (≥90%), highlighting areas where the depth-dependent velocity structure closely matches the corresponding terrane. Major tectonic boundaries, coastline, and mapped faults are overlain for reference; symbology follows **Fig. 1**. The four panels illustrate the lateral partitioning of velocity structure among terranes and the offshore–onshore and along-strike variability resolved by the similarity analysis.

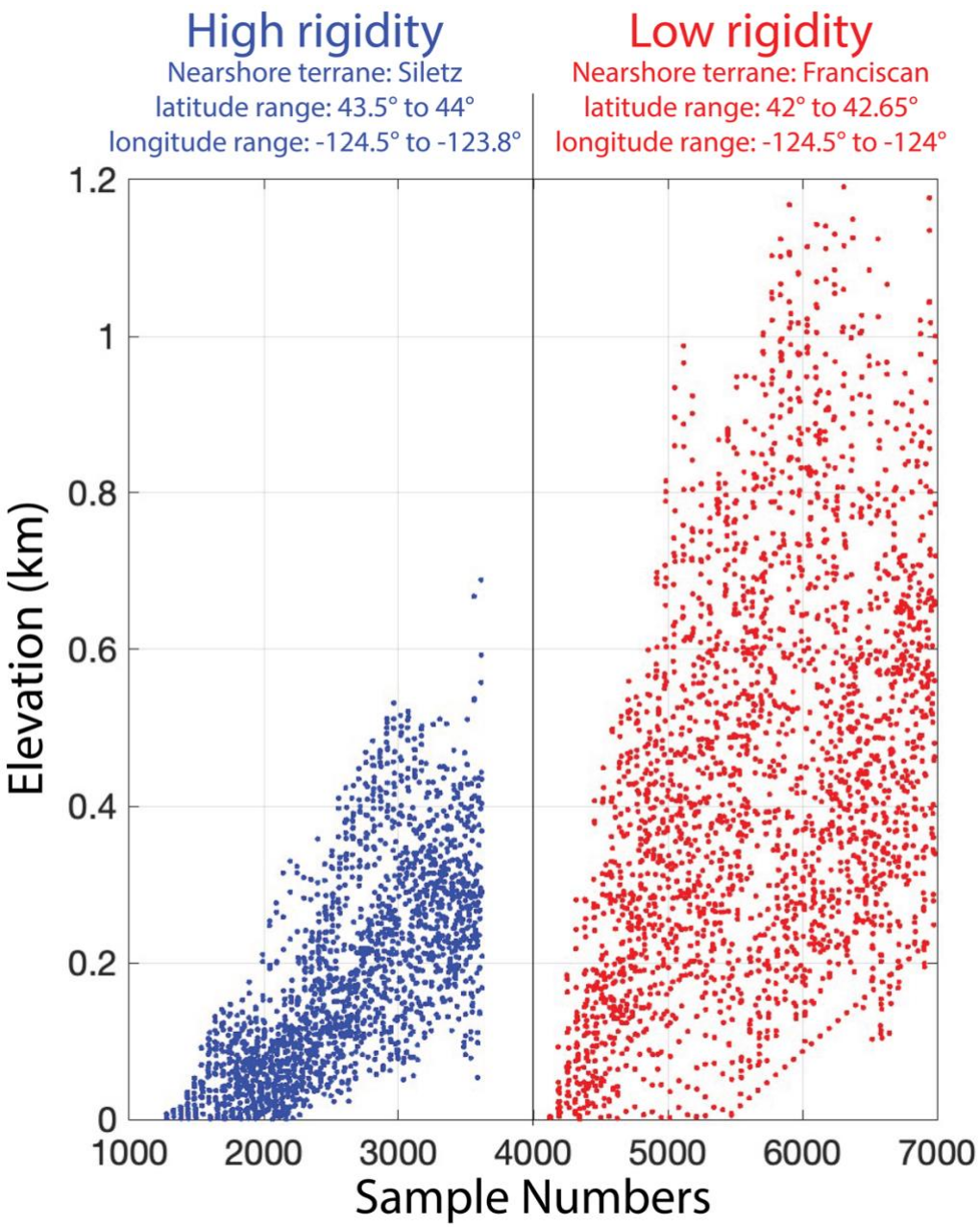

Fig. S9.
Elevation distributions of high- and low-rigidity onshore regions. Comparison of topographic relief between the Siletz terrane (high rigidity; blue) and the Franciscan terrane (low rigidity; red). Data were sampled at a 0.01° interval across the latitude and longitude ranges specified at the top of the figure. The Franciscan domain exhibits significantly higher topographic relief, with elevations exceeding 1.1 km, compared to the Siletz domain which remains mostly below 0.5 km.

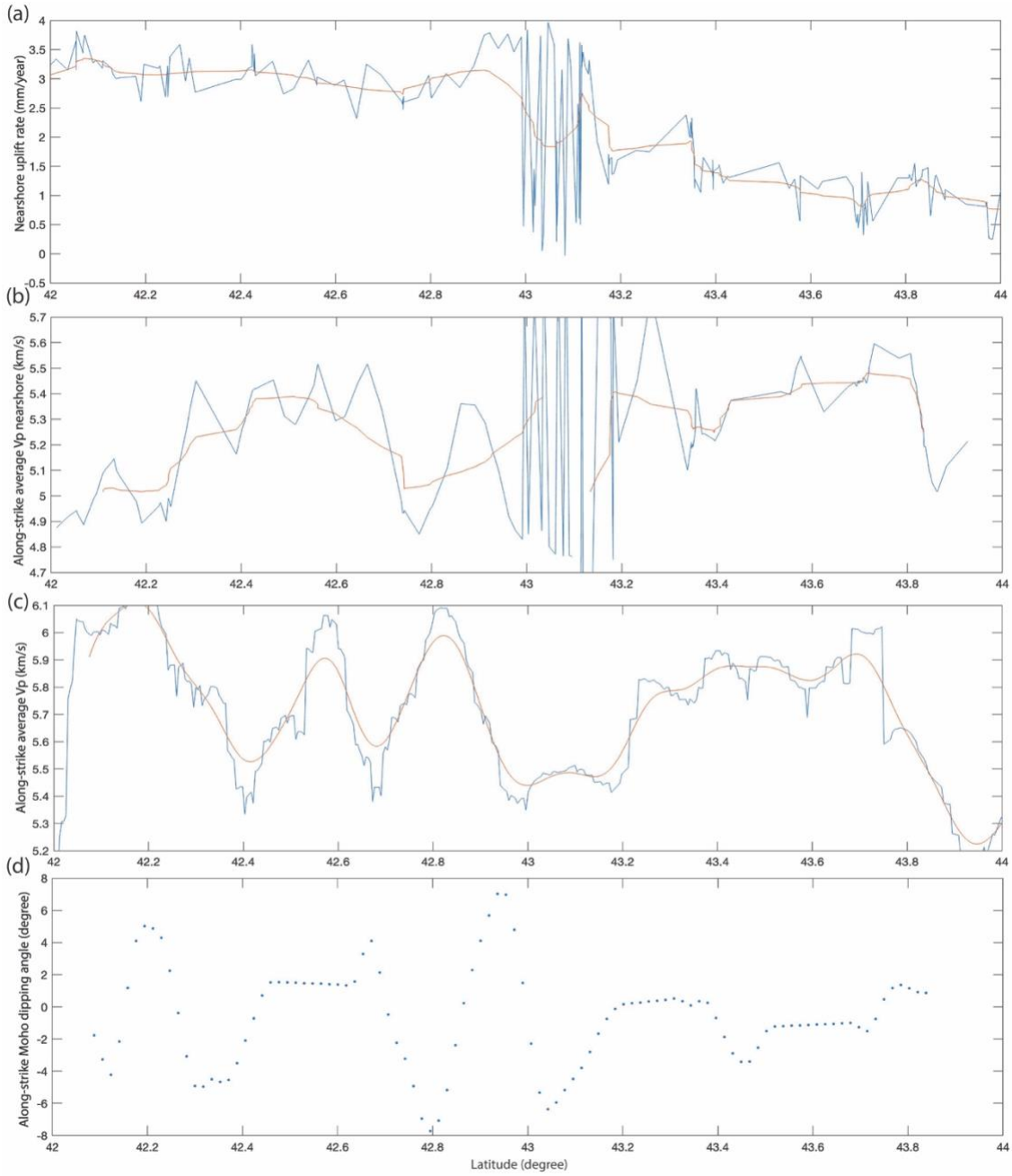

Fig. S10.
Calculation of different trends along-strike direction of the subducting slab. Values are averaged within each latitude interval (blue lines in panels a–c; blue dots in panel d). For panels a–c, a smoothed mean trend is also shown (orange line), obtained by applying a Gaussian mean to the averaged values. Only these mean trends are shown in **Fig. 5**. The y-axis labels in each panel indicate the corresponding data type. See the caption of **Fig. 5** for a detailed description of the datasets.

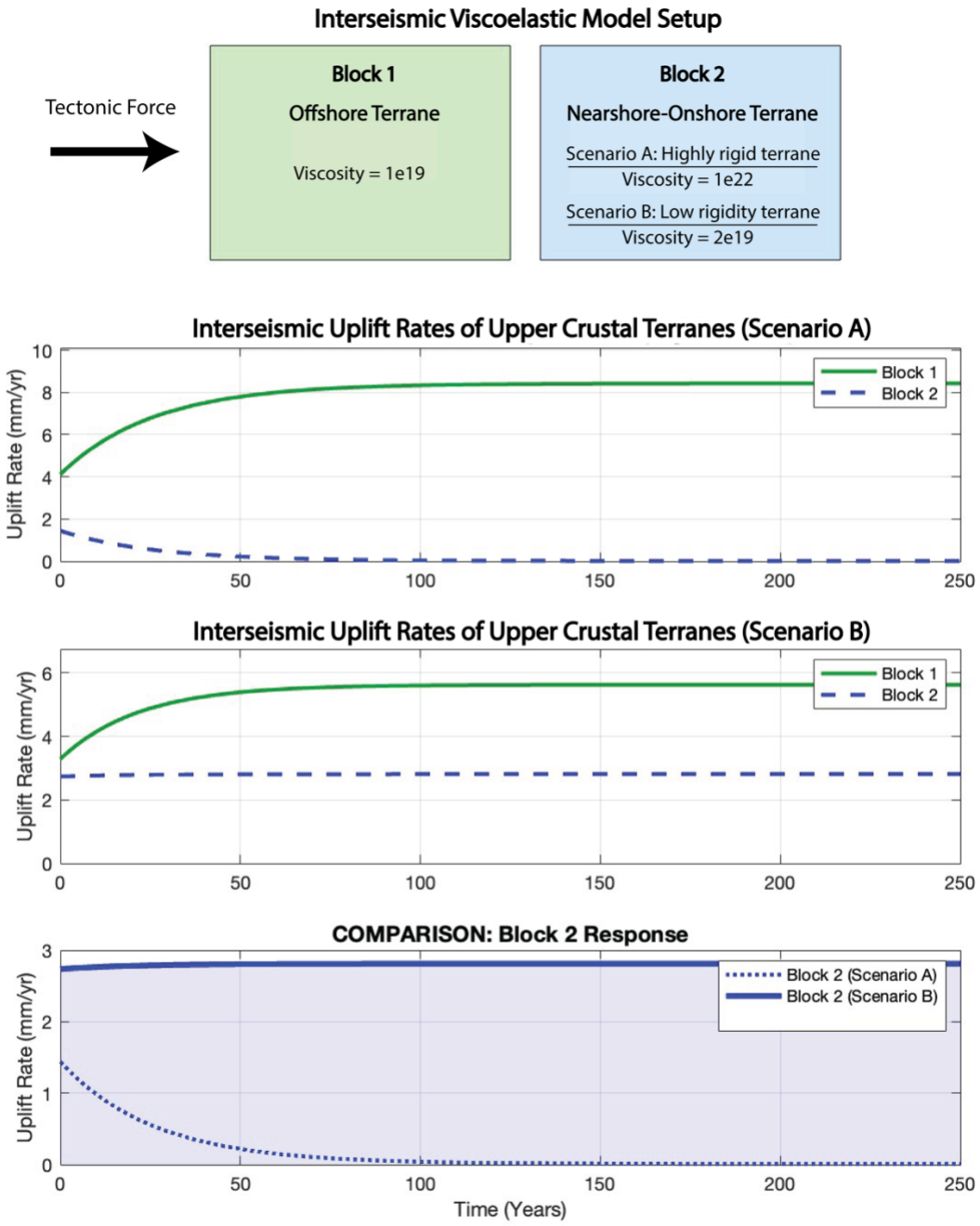

Fig. S11.
Dynamic force evolution and time-dependent uplift response in a two-block Maxwell viscoelastic model of the forearc. Top panel illustrates the model setup, in which an offshore terrane (Block 1; viscosity = 10^{19} Pa·s) and a nearshore–onshore terrane (Block 2) are mechanically coupled and subjected to constant tectonic forcing representing interseismic convergence. Two rheological scenarios are explored for Block 2: (A) a high-rigidity terrane (viscosity = 10^{22} Pa·s) and (B) a low-rigidity terrane (viscosity = 2×10^{19} Pa·s). Middle panels show the time evolution of uplift rates for each block over a 250-year interseismic interval. The bottom panel compares the uplift response of Block 2 between scenarios, illustrating how contrasts in Maxwell relaxation time govern interseismic strain partitioning.

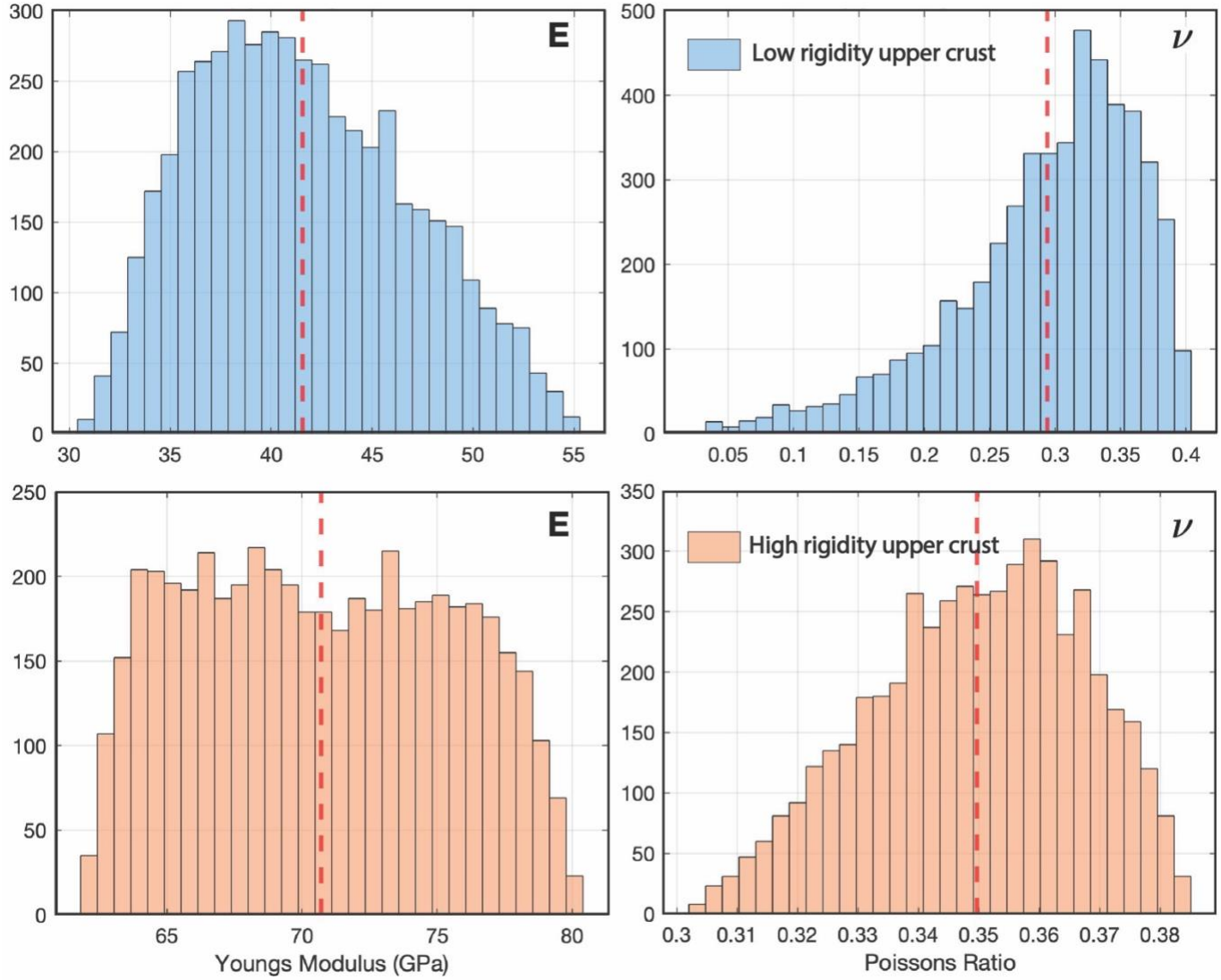

Fig. S12.
Distributions of elastic parameters in Monte Carlo simulations based on tomography-derived Vp range. Histograms show the range of Young's modulus (E) and Poisson's ratio (ν) sampled for the low-rigidity (top row, blue) and high-rigidity (bottom row, orange) upper-crustal domains.

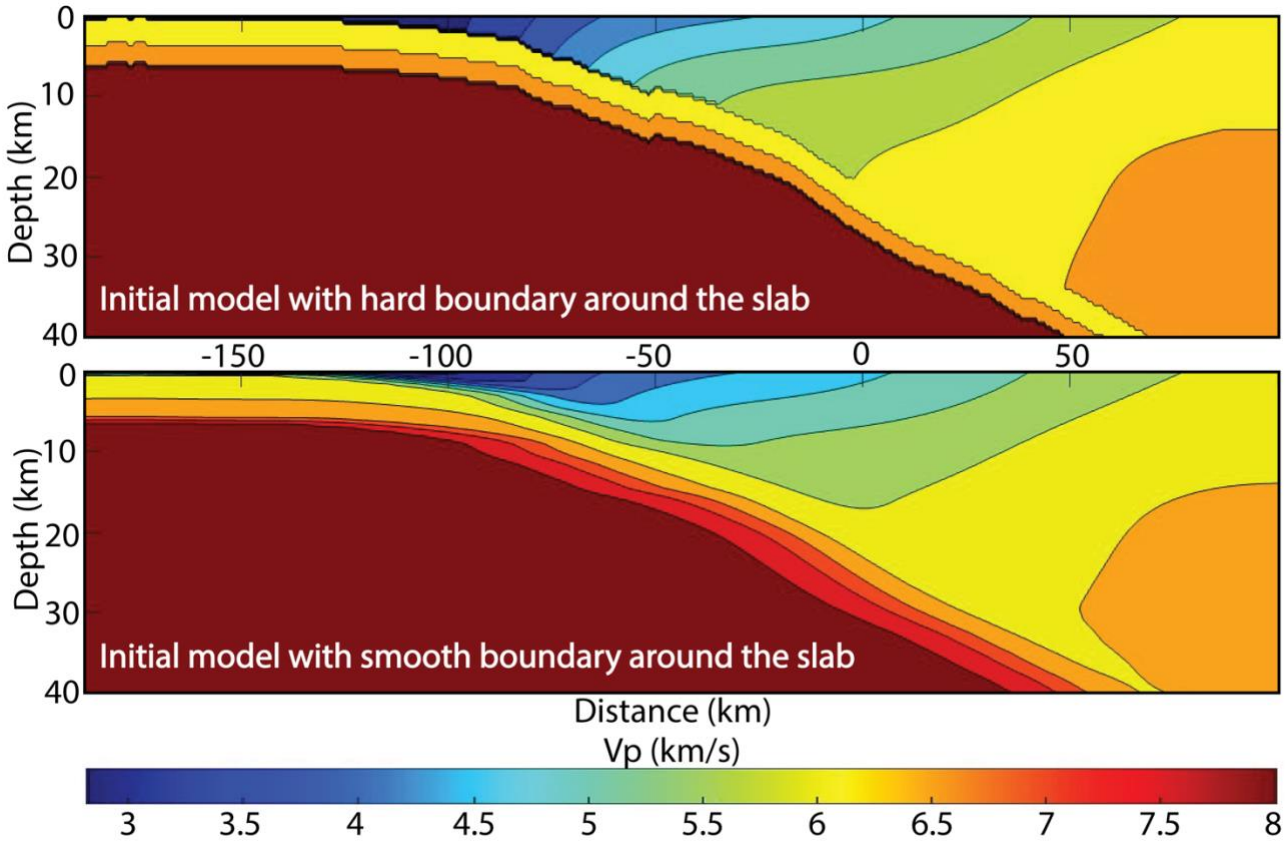

Fig. S13.
Initial velocity models used for the tomographic inversion. Top section shows initial model with a hard, step-like velocity boundary imposed at the slab interface. Bottom section shows the initial model in which velocity contrasts around the slab are smoothed by convolving the upper part of the model with a moving-average filter, producing a gradual transition across the slab interface. The smoothed initial model is adopted to reduce artificial gradients at sharp boundaries and to ensure stable convergence of the inversion without prescribing slab geometry a priori.

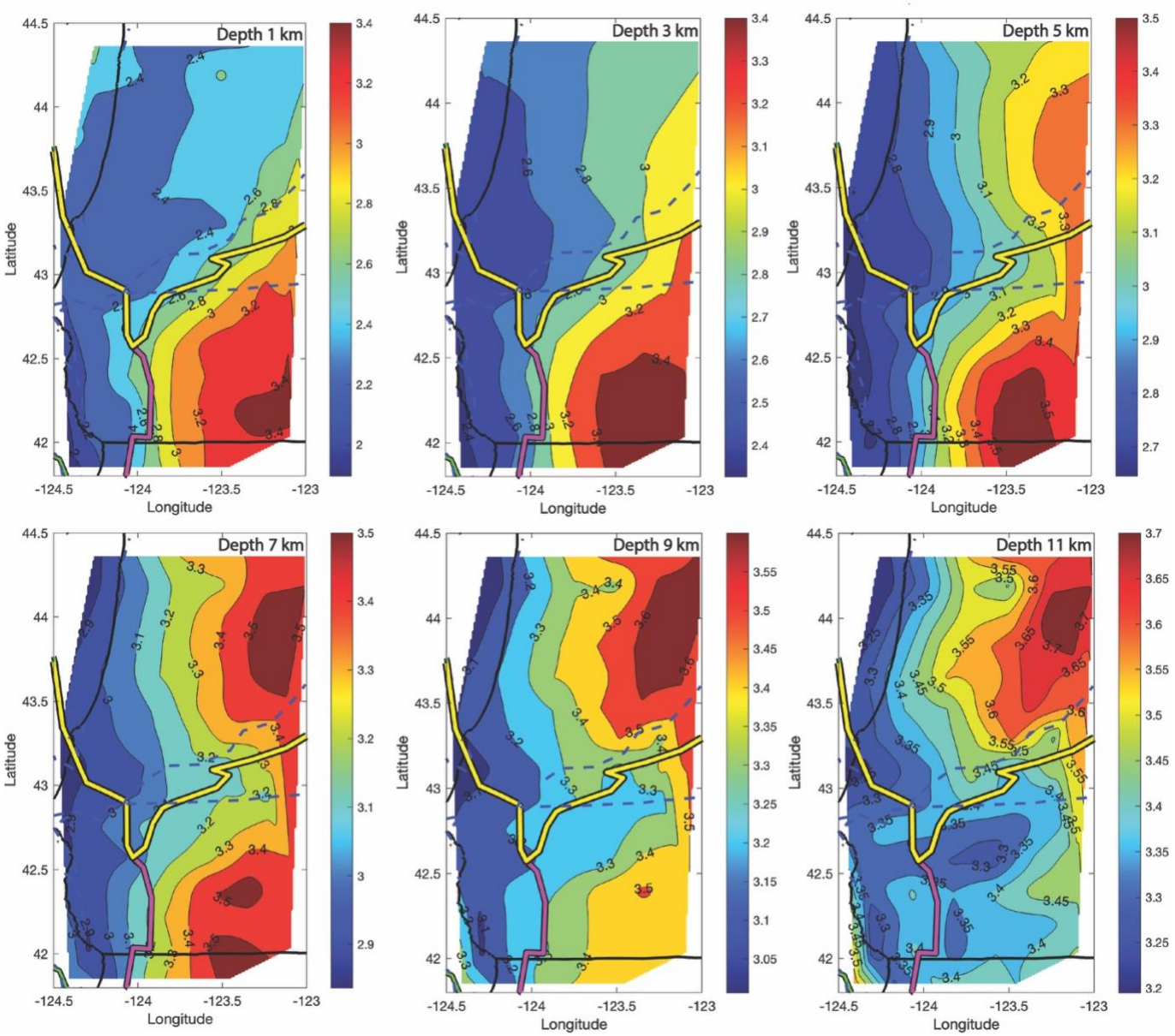

Fig. S14.
S-wave velocity (Vs) maps in our study area from the regional model of the Cascadia Region Earthquake Science Center.